Structural and mechanistic insights into Main protease (Mpro) dimer interface destabilization inhibitor: Unveiling new therapeutic avenues against SARS-CoV-2

Ankur Singh[1], Kuldeep Jangid[1], Sanketkumar Nehul[1], Preeti Dhaka[1], Ruchi Rani[1], Akshay Pareek[1], Gaurav Kumar Sharma*[2], Pravindra Kumar*[1], Shailly Tomar*[1]

[1]Department of Biosciences and Bioengineering, Indian Institute of Technology, Roorkee, Uttarakhand (247667), India

[2] Indian Veterinary Research Institute, Izatnagar, Bareilly, Uttar Pradesh - 243122, India

ABSTRACT: SARS-CoV-2 variants recurrence has emphasized the imperative prerequisite for effective antivirals. The main protease (Mpro) of SARS-CoV-2 is crucial for viral replication, making it one of the prime and promising antiviral target. Mpro features several druggable sites, including active site and allosteric sites near the dimerization interface that regulate its catalytic activity. This study has identified six highly efficacious antiviral SARS-CoV-2 compounds (WIN-62577, KT185, bexarotene, ledipasvir, diacerein, and simepervir) using structure-based virtual screening of compound libraries against Mpro. Using SPR and ITC, the binding of selected inhibitory compounds to target Mpro was validated. FRET-based protease assay demonstrated that the identified molecules effectively inhibit Mpro with IC_{50} values in the range from 0.08 to 7.31 μM. Additionally, *in-vitro* cell-based antiviral assays showed high efficacy with EC_{50} values in the range of 1.8 to 18.92 μM. Crystal structure of Mpro-minocycline complex detailed the possible inhibition mechanism of minocycline, an FDA-approved antibiotic. Minocycline binds to an allosteric site, revealing residues critical for the loss of protease activity due to destabilization of molecular interactions at the dimeric interface, which are crucial for Mpro proteolytic activity. The study suggests that the binding of minocycline to the allosteric site may play a role in Mpro dimer destabilization and directs the rational design of minocycline derivatives as antiviral drugs.

Keywords: SARS-CoV-2, Main protease, dimer interface inhibitors, antivirals.

INTRODUCTION

The mysterious outburst of coronavirus disease 19 (COVID-19) in Wuhan, China, in late 2019 has drawn attention of the world's scientific community.[1] Earlier epidemics of severe acute respiratory syndrome coronavirus (SARS-CoV) in Guangdong, China, in 2003 and Middle East respiratory syndrome coronavirus (MERS-CoV) in 2013 have shown a high decease rate.[2] Coronaviruses have spread cross-species transmission in both outbreaks, infecting humans and other vertebrates.[3] The occasional recurrence of coronavirus has proved to be a substantial global threat to human lives.[4] Irrespective of vaccine's prominent success, the viral genome's unpredictable mutations raised questions about the efficacy of available vaccines.[5,6] Predominantly, the Omicron and its lineages carry more than 30 mutations in spike protein, primarily targeted for vaccine development.[7] These mutations cause predominant conformational deviations in the spike protein, empowering the virus to evade the immune

response produced by current vaccines and sustained viral growth.[8] Therefore, targeting other crucial viral proteins for drug discovery becomes indispensable.

SARS-CoV-2 has a genome size of ~30 kb with 12 open reading frames (ORFs). The genomic organization is in order 5'-replicase (rep)-spike (S)-envelope (E)-membrane (M)-nucleocapsid (N)-3' and short untranslated regions.[9] The *rep* gene covers almost two-thirds of the genome and encodes two overlapping polyproteins, pp1a and pp1ab, using ORF1a and ORF1b.[10] Papain-like protease (PLpro) and Mpro cleave the replicase polyprotein into 16 functional non-structural proteins (nsps), crucial in genome transcription and replication.[11,12] Mpro cleaves at different sites (nsp4-nsp16) in downstream polyproteins to form individual mature proteins.[13]

Mpro functions as a homodimer, with two monomers situated closely perpendicular to each other.[14,15] Each monomer encompasses three main domains: Domains I (residues 10–99), domain II (residues 100–182), and domain III (residues 198–303).[15] Domain I & II consist of a six-stranded antiparallel β-barrel fold and form a chymotrypsin-like structure, keeping the active site in the cleft between these domains.[16] The fundamental cleavage motif of Mpro is Leu Gln↓(Ser/Ala/Gly), which is conserved amid several variants of SARS-CoV-2.[15] Domain III is a C-terminal helical domain, which is vital for protein dimerization and regulation using an intermolecular salt-bridge interface between Glu290 and Arg4.[17] The complexities of dimer dynamics showed that Mpro works on a flip-flop mechanism where only one monomer remains active at a time.[18] Mpro functions as an asymmetric dimer, potentially exhibiting a half-site acylation-deacylation catalytic cycle. In this cycle, when one subunit adopts the active acylated state, the other subunit enters the deacylated state, and they alternate between these states.[18,19] Targeting/mutating the key residues in the dimeric interface can significantly impede protease activity, which profoundly relies on suitable dimerization and the accurate alignment of the subdomains.[18,] In fact, Mpro has six experimentally confirmed allosteric sites together with dimeric site.[20] The residues involved in these sites are highly conserved among SARS-CoV-2 variants, which advocates them as prime drug targets against SARS-CoV-2.[21] Gunther et al. performed X-ray screening to discover potential drugs against Mpro and identified five compounds that also interact to two discrete allosteric sites.[22] Numerous potential inhibitors of SARS-CoV-2 Mpro are reported, but most of them fall into the peptidomimetics category, which repeatedly illustrates reduced pharmacokinetic (PK) properties. Therefore, considering the multiple roles of Mpro and targeting both the active and allosteric sites may provide a propitious approach for developing safe and effective antivirals against pan SARS-CoV-2 variants.

The present study reports the *in-silico* screening of FDA-approved drug library (Selleckchem), natural compound library (Selleckchem), and LOPAC^{1280} (Library of Pharmacologically Active Compounds, Sigma-Aldrich, St. Louis, MO) library against the substrate-binding pocket and allosteric site (dimeric interface) residues of Mpro. The residues that form the substrate binding site and dimeric interface site are essential for catalytic activity and are conserved across various SARS-CoV-2 variants and SARS-CoV strains of *Coronaviridae* family.[23,24] The molecular docking and molecular dynamics (MD) simulations

were successfully performed to ascertain sixteen potential antiviral compounds. Further, twelve out of these compounds were biophysically and biochemically validated using surface plasmon resonance (SPR), isothermal titration calorimetry (ITC) and fluorescence resonance energy transfer (FRET)-based protease assay. Subsequently, site-directed mutagenesis (C145A and E290A) helped to examine the mutational effects on the enzyme activity and were used a s control for experiments. Afterward, an *in vitro* cell culture-based antiviral assay was performed to find the most efficacious compounds with significant antiviral against SARS CoV-2. Notably, the Mpro-minocycline crystal structure revealed that the compound binds to an allosteric site near the dimeric interface of Mpro and complex structure analysis revealed structural changes that destabilize and make Mpro inactive. The compounds reported in this study as potential antivirals are recommended as leading novel Mpro inhibitors against different SARS-CoV-2 variants for further investigations and *in vivo* validation.

MATERIALS AND METHODS

Structure-based virtual screening of drug libraries. To identify new potential antivirals targeting enzyme activity and dimer interface of Mpro (Protein Data Bank, PDB id: 6LU7),[25] virtual screening was conducted using PyRx 0.8.[26] The pharmacologically active compounds for this screening were sourced from the FDA-approved drug library (Selleckchem), the natural compound library (Selleckchem), and the LOPAC^{1280} drug libraries, all in the Structured Data File (SDF) format. Over 20,000 compounds were subjected to high-throughput virtual screening analysis. Energy minimization and file format conversion of molecules into the Autodock ligands (.pdbqt) format were performed using PyRx 0.8.[26] Subsequent screening of the selected molecules against potential binding sites of the SARS-CoV-2 Mpro protein was conducted using PyRx 0.8 in conjunction with AutoDock Vina.[27,28] The grid center points for the active site region were set at X = -24.91, Y = 12.33, Z = 57.43, with box dimensions of 48.30 Å × 69.97 Å × 60.87 Å. The grid centre points for the dimeric interface region were set at X = -24.92, Y = 15.19, Z = 51.60, with box dimensions of 24.80 Å × 23.68 Å × 27.61 Å with an exhaustiveness level of 8.

Designing of Mpro substrate peptides. SARS-CoV-2 Mpro specifically cleaves the non-structural polyproteins at designated cleavage sites. Using the Weblogo 3 web server version 3.7.4,[29] a multiple sequence alignment (MSA) of various cleavage sites reveals that the residues of Mpro substrates are highly conserved at specific positions (Supporting information, Figure S1). Based on published studies that have utilized octapeptides as inhibitors following the "distorted key" approach[30], a substrate peptide consisting of eight residues was selected. The octapeptide is named after Schechter and Berger's (1967) nomenclature, which states that protease cleaves between P1 and P1' amino acids.[31] Therefore, eleven octapeptides, designated as Pep1 through Pep11, were considered as reference molecules in molecular docking analysis. These Mpro octapeptide substrates were designed using PyMOL 2.3 software[32] to explore the binding efficacy of the substrates to the Mpro active site (Supporting information, Table S1).

Molecular docking of top-hit compounds and octapeptides. The screened compounds with higher binding energy than the octapeptide substrates (cleavage sites between different nsps) were docked using AutoDock 4.2.6. During the docking procedure, Kollman

charges were added, hydrogens were introduced, and water molecules were removed from the protein structure using AutoDock MGL Tools 1.5.6.[33] Hence, the protein was saved in .pdbqt file format. The .pdbqt file format of the top hits ligands were retrieved from PyRx 0.8 directory, and the .pdb file format of octapeptides were designed using PyMOL 2.3. The dimensions of grid box and centre point coordinates were kept same as per virtual screening parameters. Combined with the Lamarckian Genetic Algorithm (GA), the grid-based energy evaluation method was used for docking studies. Autodock 4 was used to select the maximum number of evaluations (250,000,000) with a total number of 50 GA runs by keeping other docking parameters as default**.**

To analyze the conformational changes of protein atoms in both free and ligand-bound states, Molecular Dynamic (MD) simulations were conducted within a defined hydration environment for 100 nanoseconds using the Gromacs 5.1.4 suite.[34,35] The CHARMM36m force field was applied on a LINUX-based workstation.[36] The dynamic flexibility of sixteen ligands at the Mpro active and allosteric sites was examined. Ligand topology was generated using Avogadro software,[37] and the protein-ligand complexes were solvated with simple point charge (SPC) water in a 534.76 nm^3 cubic box. Na+ ions were added to neutralize the system. Energy minimization was carried out using steepest descent and conjugate gradient algorithms, while the LINCS (LINear Constraint Solver) algorithm applied to calculate covalent bond constraints. The system was equilibrated at 300K through NVT and NPT phases using the Parrinello-Rahman method with a 2 femtosecond (fs) timestep. Short-range Lennard-Jones and Coulomb interactions were calculated with a 12 Å cutoff, while long-range electrostatic interactions were assessed using the particle mesh Ewald method with a Fourier grid spacing of 0.16. The system was equilibrated for 100 picoseconds under NPT and NVT conditions, followed by a 100 ns MD simulation with a 2 fs timestep. Commands were used to analyze RMSD, RMSF, radius of gyration, and solvent-accessible surface area (SASA).

SARS-CoV-2 Mpro expression and purification. The plasmid containing the gene for the SARS-CoV-2 Mpro protease (Mpro, Replicase polyprotein 1ab residues 3264-3569, UniProtKB accession: P0DTD1) was kindly provided by Professor Manidipa Banerjee's lab at the Kusuma School of Biological Sciences, Indian Institute of Technology Delhi (IIT Delhi), India. This plasmid was used as a template for gene amplification using PCR and cloned into the pET28c vector. The pET28c plasmid with Mpro gene was confirmed through DNA Sanger sequencing. The recombinant Mpro plasmid was used to express the Mpro protein using BL21 DE3 cells. For protein expression, the culture was grown at 37°C and 180 rpm until the optical density at 600 nm reached 0.6-0.8. The cells were then shifted to 16°C, induced with 2.5 mM IPTG, and incubated for 16-18 h at 180 rpm. The cells were garnered by centrifugation (6000 rpm at 4°C for 10 min) and resuspended in lysis buffer (50 mM Tris-HCl, pH 8.0, 150 mM NaCl). The cells were then homogenized using a French press (Constant Systems Ltd, Daventry, England), and cellular debris was removed by centrifugation at 10,000 rpm for one h at 4°C. The nickel-nitrilotriacetic acid (Ni-NTA) beads was pre-equilibrated using binding buffer (50 mM Tris-HCl, pH 8.0, 150 mM NaCl) and the clarified supernatant was loaded onto this beads in a gravity flow column. The flowthrough was collected and beads was washed with binding buffer. The recombinant Mpro protein was eluted using 20-160 mM imidazole in

binding buffer. A single band was observed of ~33 kDa size in ~15% SDS-PAGE that confirmed the purity of the Mpro protein [Supporting information, Figure S2(a)]. Mpro fractions containing ~pure sample were pooled and dialyzed against buffer containing 20 mM HEPES, pH 8.0, 20 mM NaCl. Protein was concentrated using Amicon filters with a 10 kDa molecular weight cutoff for subsequent biophysical and biochemical assays, as well as for protein crystallization. The mutants (E290A and C145A) were generated using the native Mpro plasmid as a template by site-directed mutagenesis using an overlapping PCR strategy with synthetic primers. The expression and purification of both the mutants was done using the same protocol as that of the wild-type Mpro mentioned above [Supporting information, Figure S2(b and c)].

Determination of binding affinity using SPR. The selected potential Mpro inhibitory molecules were assessed for their binding affinity with purified SARS-CoV-2 Mpro protein using Biacore T200 SPR instrument (GE Healthcare). SPR experiments to validate molecular interactions between analyte, the inhibitory molecules and the ligand Mpro were performed at 25 °C. The running buffer comprised of 0.1% (v/v) dimethyl sulfoxide (DMSO), 20 mM Tris-HCl (pH 8.0), and 20 mM NaCl. The NTA (Nickel-charged Nitrilotriacetic Acid) chip was employed to immobilize the histidine-tagged Mpro protein. The channel 1-2 of Biacore NTA chip surface was activated using the running buffer, and then 20 µM purified Mpro was immobilized at a surface density varying between 400 and 500 response units. For determining the binding affinity, the solution of small molecules in the range of 10-1000 µM increasing concentrations were applied and passed over the chip surface in experimental channel 2 and reference channel 1 at a 30 µL/min flow rate for 60s Following that, the running buffer was flown at a rate of 30 µL/min for 120 s for recording the dissociation rate of the molecules from protein ligand. The equilibrium dissociation kinetic constants (K_D) for each molecule were obtained by evaluating the SPR data using a single-cycle kinetic method of Biacore T200 evaluation software V3.0. Sensogram fitting was carried out with the 1:1 Langmuir binding model via BIAcore T200 evaluation software.

Thermodynamics of Mpro dimerization and destabilization by inhibitors. ITC experiments are conducted to quantify the heat associated with dissociating Mpro dimers into monomers, both in the absence of inhibitors and in the presence of increasing concentrations of small molecule inhibitors. ITC measurements were performed by Microcal-ITC200 instrument (Malvern, Northampton, MA) at 25°C. Purified Mpro protein was meticulously dialyzed against buffer A (20 mM HEPES, pH 7.4, and 20 mM NaCl) and degassed prior to preforming ITC experiments. The stock solutions of inhibitors in 1-5% DMSO were diluted to the desired concentration in buffer A. To determine the equilibrium in monomer-dimer states by doing dilution ITC experiments of Mpro, primarily, the sequential injections of concentrated (100 µM) Mpro protein were stirred into the calorimeter cell (270 µl) initially containing buffer alone, with an atypical injection sequence of 16×2µl at 220-sec intervals. To analyse Mpro dimer destabilization in the presence of inhibitors, 100 µM Mpro was preincubated with varying concentrations of inhibitors at 25°C for 30 min, followed by its titration against buffer A kept in the calorimetric cell. The control titration of inhibitors in buffer A against buffer A kept in the calorimetric cell showed negligible heat change response. The reference cell was

filled with buffer, and the reference power was set to 10 µcal/s. Experiments were performed at a stirring speed of 850 rpm at an initial delay of 100 sec. The obtained isotherms were fitted into one-site binding model using MicroCal Origin 7.0 analysis software.

Assessment of Mpro inhibition using *in vitro* FRET-based proteolytic assay. To determine *in vitro* protease activity of purified SARS-CoV-2 Mpro and to measure the inhibitory potential of identified compounds, a fluorescence resonance energy transfer (FRET)-based protease assay was used. A fluorogenic peptide substrate AVLQ↓SGFR-Glu (Biolinkk, India) comprising 4-(4-dimethylaminophenyl-azo) benzoic acid (DABCYL) and 5-[(2-aminoethyl) amino] naphthalene-1-sulfonic acid (EDANS) at its N- and -C terminus respectively, where DABCYL acts as quencher and EDANS acts as fluorophore was used to determine the enzymatic activity of Mpro. The close proximity of the quencher and fluorophore does not allow the substrate to exhibit a higher fluorescence signal; however, the active Mpro is expected to cleave the substrate peptide and exhibit augmented fluorescence signals with excitation at 360 nm and emission at 460 nm. The assay was executed in 96-well, flat-bottomed, black plates (Corning) comprising of assay buffer containing 20 mM HEPES (pH 7), 0.5 mM EDTA, 1 mM dithiothreitol, 5% glycerol) with 100 µl final volume in each well. For enzyme inhibition reactions, Mpro (1 µM) was incubated with different concentrations of compounds ranging from 0.1 µM - 100 µM at 22 °C for 1 h and then dispensed into a 96-well plate. The reactions were set up in triplicates. 10 µM substrate was added to each well to initiate the reaction, and the fluorescence signals were measured with excitation at 360/40 nm and emission wavelengths of 460/40 nm using a multimode microplate spectrophotometer (Biotek Synergy H1 Hybrid). FRET based protease assay for both the mutants was also performed to investigate the change in enzymatic activity comared with native Mpro. The initial velocities of triplicate data were averaged and determined using the linear part of the reaction curves, whereas the 50% inhibition (IC_{50}) concentrations of inhibitors were calculated using a dose-response curve through nonlinear regression with a variable slope using GraphPad Prism 9.0.

Virus propagation and cells. The wild-type SARSCoV-2/Human/IND/CAD1339/2020 strain (GenBank accession no: MZ203529) was passaged in Vero cells, and the supernatant was collected and clarified by centrifugation before being aliquoted for storage at −80 °C. The virus titer in terms of $TCID_{50}$ was measured in Vero cells following end-point dilution method. Vero cell lines used in this study were procured from NCCS (Pune, India). The cell line was maintained in high glucose Dulbecco's-modified essential media (DMEM; HiMedia, India) augmented with 10% heat-inactivated fetal bovine serum (FBS; Gibco, USA), 100 units of penicillin/mL, and 100 µg streptomycin/mL (Himedia). All virus culture procedures were conducted in a Biosafety Level 3 (BSL3) facility at the Indian Veterinary Research Institute (IVRI) in Izatnagar, Bareilly, adhering to standard institute bio-safety guidelines.

Cytotoxicity assay of Mpro inhibitors. The cytotoxic potential of the identified compounds on the Vero cell line was evaluated using the MTT assay (3-[4,5-dimethylthiazol-2-yl]-2,5 diphenyl tetrazolium bromide), as previously described.[38] Briefly, Vero cells (1×10^4 cells/ well) were seeded in 96 wells plate one day prior to MTT assay. The next day, the cells were treated with 2-fold serial dilutions of the compounds, ranging from 100 µM to 1.5 µM,

for a duration of 48 hours. After the incubation period, MTT was added for the formation of formazan crystals, which were dissolved in DMSO and plate reading was taken at 570 nm. The percentage cell viability of compound-treated cells was calculated by comparing the readings with only solvent (DMSO) treated cells.

Antiviral efficacy of Mpro inhibitors. Antiviral activity of compounds was evaluated by detecting the reduction in Viral load in the presence of compounds as compared to control-infected Vero cells, using quantitative reverse transcription-polymerase chain reaction (qRT-PCR) as previously described.[38] Briefly, Vero cells were cultured in 24-wells plate in DMEM media supplemented with 10% FBS and 100 units of penicillin and 100 µg streptomycin/mL at 37 °C and 5% CO_2. Depending on their solubility, drug stocks were made in either dimethyl sulfoxide (DMSO) or water. Three hours of pre-treatment of two-fold decreasing concentration of compounds in DMEM (2% FBS) was given to cells before infection. After pre-treatment, the cells were washed with PBS and then infected with SARS-CoV-2 at a Multiplicity of infection (MOI) of 0.01 in DMEM for 1.5 h for virus attachment. After incubation, the viral inoculum was removed, and the cells were washed with PBS before being replenished with fresh medium containing various dilutions of the compounds. At 48 hours post-infection (hpi), the plates were frozen at -80ºC. The plate was thawed the next day, and viral RNA was extracted from the cell lysate of cells using HiPurA™ Viral RNA Purification Kit (Himedia), according to the manufacturer's instructions. One-step qRT-PCR assay was performed as mentioned previously.[38] qRT-PCR was performed in duplicates. Percentage inhibition was calculated based on ΔΔCt. A graph of percentage inhibition versus concentration was plotted to determine the EC_{50} values using linear regression.

Crystallization, data collection and structure determination. Mpro was concentrated to approximately 20 mg/mL and prepared for crystallization. Crystals of Mpro were grown using the vapor-diffusion method in 96-well sitting drop plates (Hampton Research) at 293 K. Diffraction-quality crystals were obtained in a solution of 24% PEG 4000, 100 mM HEPES (pH 7.5), and 3% DMSO. For data collection, the crystals were cryoprotected with a reservoir solution containing 20% ethylene glycol and then flash-frozen in a nitrogen stream at 100 K. Mpro complexes with minocycline were prepared by soaking the crystals in cryoprotectant solutions with 2 mM minocycline for 5 minutes at 25°C before freezing and data collection. X-ray diffraction data for the Mpro-minocycline complex were collected at the home source in the Molecular Crystallographic Unit (MCU) at the Institute Instrumentation Centre (IIC), and Data quality was assessed using AIMLESS, as implemented in autoPROC.[39]

The dataset for the Mpro-minocycline complex was collected at a resolution of 2.7 Å. The initial phase of Mpro was determined by molecular replacement using MolRep[40] within the CCP4i suite,[41] with the coordinates of the apo-Mpro structure (PDB ID: 7ALH)[42] serving as the template. Iterative refinement was carried out with Refmac5[43] in the CCP4i suite, and model rebuilding was conducted using COOT,[44] followed by the incorporation of ligands and solvent. The stereochemical quality of the refined models was the incorporation MOLPROBITY[45] within Phenix.[46] Figures were generated using PyMol.[32] Data collection and refinement statistics are detailed in Table 3.

RESULTS

Mpro inhibitors identification and characterization. Using a structure-based approach to identify Mpro inhibitors, the available crystal structure of Mpro (PDB ID: 6LU7)[25] was employed for virtual screening. This screening was performed across three different small molecule compound libraries: FDA-approved drugs, natural compounds, and LOPAC[1280], using the PyRx 0.8 software.[26] Ligand molecules that bound to the active site of Mpro and the dimer interface with higher affinity than the substrate octapeptides were selected. Each ligand showed nine different poses while screening through PyRx 0.8. The top twenty-five compounds were selected through virtual screening based on their binding affinities. Further, these compounds were selected based on Lipinski's rule of five and the binding energy in the range from -10.23 to -6.4 kcal/mol. Among these, the ten most favourable top-hit compounds (etoposide, BMS-195614, KT185, idarubicin, GSK121015A, WIN-62577, eptifibatide acetate, KT203, SB 202190, and linopiridine) were selected against the active site and other top six compounds (simeprevir, minocycline hydrochloride, ledipasvir, diacerein, bexarotene, and diacerein) were targeting the dimeric interface region of Mpro. These screened molecules were employed for docking with Mpro (PDB ID: 6LU7) to discover their inhibitory potential.

Molecular docking of the top sixteen selected compounds as well as eleven octapeptides, was carried out using AutoDock 4.2.6. The detailed interaction mechanisms of the P4-P4' residues of the substrate peptides are presented in [Table S(3-10)]. The predicted binding energies (B.E.) from molecular docking analysis of octapeptides ranged between -4.68 kcal/mol to -8.99 kcal/mol. These binding energies were selected as reference to select the potential compounds. The B.E. of the selected compounds was in the range of -10.23 to -6.4 kcal/mol., as given in Supporting information, Table S2, which is similar or higher than the substrate octapeptides. The interaction analysis between protein and ligand molecules were performed using PyMOL[32] (Figure 1) and LIGPLOT[+47] (Supporting information, Figure S3).

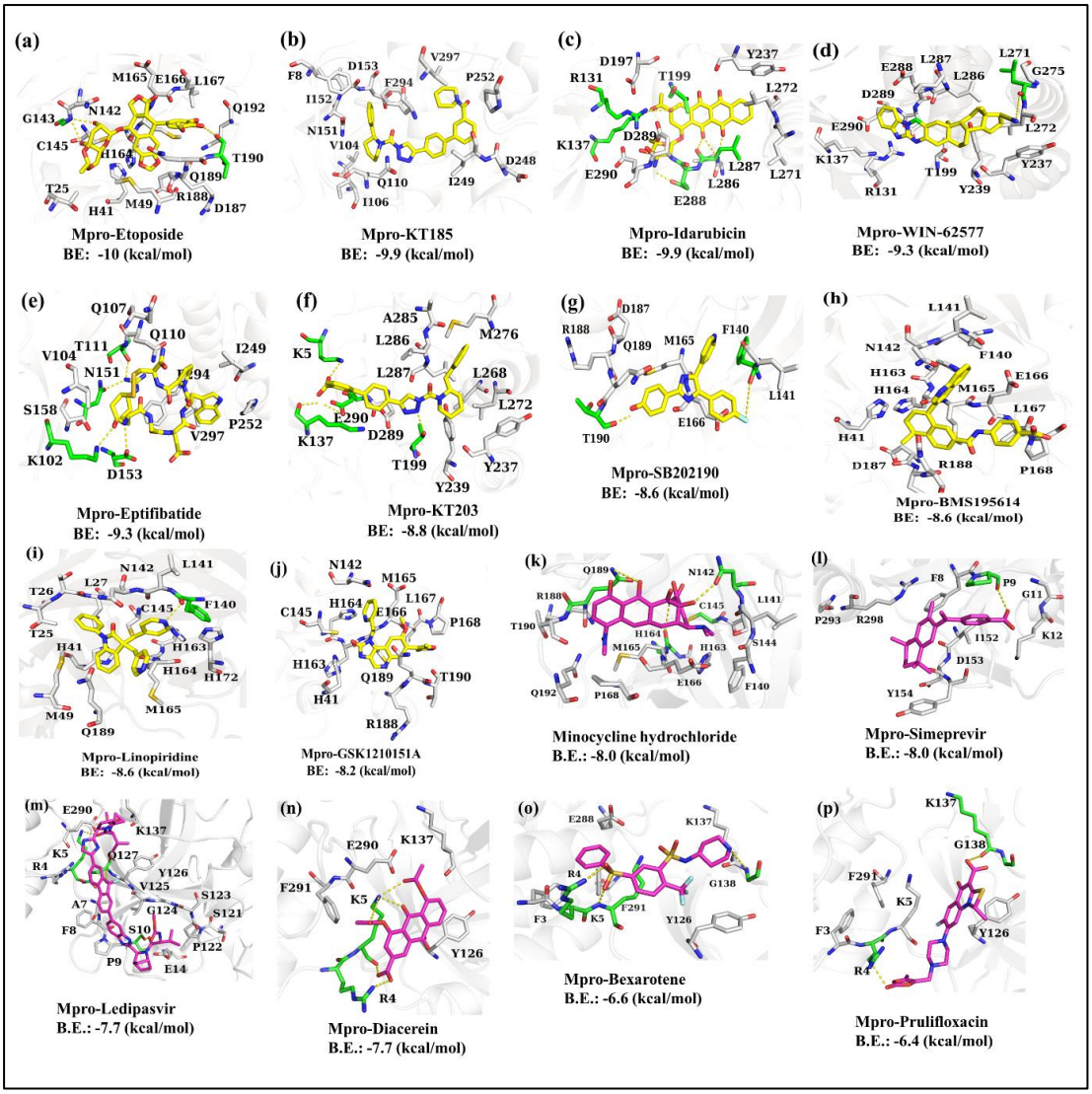

Figure 1. Molecular docking interactions and orientations of top-hit selected small molecules against substrate-binding pocket **(a-j)** and the dimeric interface (allosteric site) pocket **(k-p)** of Mpro. **(a)** Etoposide, **(b)** KT185, **(c)** Idarubicin, **(d)** WIN-62577, **(e)** Eptifibatide, **(f)** KT203, **(g)** SB202190, **(h)** BMS195614, **(i)** Linopiridine, **(j)** GSK1210151A, **(k)** Minocycline hydrochloride, **(l)** Simeprevir, **(m)** Ledipasvir, **(n)** Diacerein, **(o)** Bexarotene, and **(p)** Prulifloxacin were analysed using Pymol. In these diagrams, gray ribbons represent Mpro residues with 80% transparency, while ligands against substrate-binding pocket and dimeric interface pocket are displayed in yellow and magenta colors respectively. Green stick models highlight residues involved in hydrogen bonds (indicated by yellow dotted lines), and gray stick models represent residues involved in hydrophobic interactions.

The docking analysis of compounds with Mpro identified several key residues in the active site that are essential for interactions with potential inhibitory molecules, including His41, Phe140, Leu141, Asn142, Gly143, Cys145, His163, His164, Met165, Glu166, Leu167, Pro168, Asp187, Arg188, and Gln189. Among these, His41 and Cys145 form a catalytic dyad, which is critical for the enzymatic activity of Mpro. Furthermore, the residues His4, Ser10, Gly11, Glu14, Asn28, Ser139, Phe140, Ser147, Thr190, Glu290, and Arg298 are located at the dimer interface and play a crucial role in the formation of the homodimer. These specific residues were chosen for molecular docking studies with inhibitory compounds targeting the

dimeric interface. The interaction analysis suggests that these sixteen selected molecules could potentially inhibit the main protease of SARS-CoV-2 by binding to the catalytic site or by destabilizing the formation of the homodimer, thereby potentially block and inhibit SARS-CoV2 viral propagation.

Molecular dynamics simulation studies. The stability of ligand-bound Mpro was evaluated by analyzing the RMSD of Cα atoms through MD simulation. Molecular dynamics simulations of Mpro with the top sixteen compounds were performed using GROMACS 5.1.4. Of these sixteen compounds, ten were screened against the active site pocket of Mpro, while the remaining six were screened against the dimeric interface pocket. Except for KT185, the complexes with the top ten screened compounds against active site showed minor variations around 10 ns during the simulation and stabilized afterwards [Supporting information, Figure S4(a)]. KT185 displayed greater fluctuation until 55 ns, after which it remained stable throughout the 100 ns simulation period. RMSF analysis was performed to determine the normal deviation of protein moieties over the simulation time. In this study, the RMSF for each residue of Mpro complexed with the selected compounds was analyzed [Supporting information, Figure S4(b)]. Loop regions exhibited higher deviations compared to helices and sheets. Analysis of Mpro protein fluctuations based on RMSF indicated that regions between amino acid residues 45-55 and 179-200 and the C-terminal region showed higher fluctuations [Supporting information, Figure S4(b)]. After forming the protein-ligand complex, fluctuations in these regions significantly decreased, indicating that Mpro became more stable in the ligand-bound state.

The radius of gyration (Rg) was measured to assess changes in the compactness of the ligand-protein complex. The Rg value for the protein and protein-ligand complexes was calculated for the 100 ns trajectory [Supporting information, Figure S4(c)]. Rg results showed that the Mpro complexes with different inhibitor molecules had similar Rg values, except for KT185, which showed a slight difference at 30-40 ns but stabilized afterwards. These results demonstrated that all the given complexes are stably formed and that the protein secondary structures are highly packed throughout the simulation. Additionally, the solvent-accessible surface area (SASA) was evaluated to understand the nature of hydrophobic and hydrophilic residues of Mpro and all Mpro-ligand structures. The SASA analysis revealed that the amino acid residues of Mpro have similar SASA values compared to Mpro-ligand complexes. This confirmed that the secondary and tertiary structures of Mpro and Mpro-ligand complexes of substrate binding site maintained stability during the simulation [Supporting information, Figure S4(d)]. Keeping all the parameters same, including the force field, MD simulation analysis was also conducted for the compounds targeting the dimeric interface. However, the RMSD values of the dimeric interface compounds exhibit greater deviations, reaching up to 3 Å from the native Mpro [Supporting information, Figure S4(e)]. Ledipasvir and bexarotene displayed the highest deviations of 3 Å after 20 ns, while simeprevir and diacerein showed deviations after 50 ns. Likewise, the RMSF vthe alues for each residue in the Mpro-ligand complexes indicated increased oscillations, leading to the destabilization of Mpro's conformation. Among them, the Mpro-minocycline hydrochloride complex displayed the highest fluctuations across residues throughout the protein. Other compounds also contributed

to the destabilization of Mpro's conformation upon interaction [Supporting information, Figure S4(f)]. The radius of gyration (Rg) analysis indicated variations in compactness, with minocycline hydrochloride and simeprevir showing differences from the native Mpro [Supporting information, Figure S4(g)]. Surface Accessible Surface Area (SASA) analysis revealed that the amino acid residues of Mpro exhibited higher fluctuations in SASA values compared to Mpro-ligand complexes [Supporting information, Figure S4(h)]. This simulation analysis clearly demonstrates that the compounds against dimeric interface residues significantly destabilize the conformation of Mpro, rendering it inactive.

Surface Plasmon Resonance for binding affinities of selected compounds. The binding affinity results for eight identified compounds with Mpro revealed K_D values ranging from low to moderate micromolar levels, as shown in Table 1, except for SB-202190, which exhibited a K_D value in the high micromolar range. To evaluate the reliability of the experimental data, the uniqueness value (U-Value) parameter is typically applied to the kinetic rate constants, with values below 15 considered statistically optimal. Considering all the binding parameters, including the association constant (Ka), dissociation constant (Kd), binding affinity values (K_D), and the U-value, idarubicin, GSK-1210151A, WIN-62577, BMS19561, eptifibatide acetate, etoposide, simeprevir, minocycline hydrochloride, ledipasvir, and diacerein emerged as the most potent compounds. Ten out of twelve compounds demonstrated strong binding affinities, with K_D values of 1.7, 53.40, 56.01, 57.50, 96.89, 101, 171.8, 200.6, 207 and 268 µM, respectively. In contrast, KT185 and SB-202190 exhibited weaker binding affinities, with K_D values of 350.1 and 1000 µM, respectively (Figure 2 and Table 1). However, since the U-value for bexarotene and prulifloxacin exceeded 15, the data did not fit properly, and binding parameters could not be determined.

Table 1. Binding parameters between the SARS-CoV-2 Mpro protein and selected compounds, including association constant (Ka), dissociation constant (Kd), binding affinity values (K_D) and uniqueness value (U-value) from the SPR experiment.

S.No.	Compound Name	Association Constant [ka (1/Ms)]	Dissociation Constant [kd (1/s)]	Binding Affinity K_D (µM)	Uniqueness Value (U-value)
1	Idarubicin	$1.226* 10^5$	0.2092	1.7	12
2	GSK-1210151A	1830	0.1025	56.0	7
3	WIN-62577	7752	0.7511	96.8	9
4	BMS19561	5007	0.8599	171.0	5
5	Eptifibatide_Acetate	345.4	0.0693	200.0	9
6	Etoposide	413.0	0.1107	268.0	7
7	KT185	1400.0	0.4901	350.0	9

8	SB-202190	630.9	0.6316	1000.0	7
9	Simeprevir	3775	0.784	207.0	15
10	Minocycline hydrochloride	1040	0.0598	57.50	5
11	Ledipasvir	3773	0.3813	101	15
12	Diacerein	998.0	0.05338	53.4	3

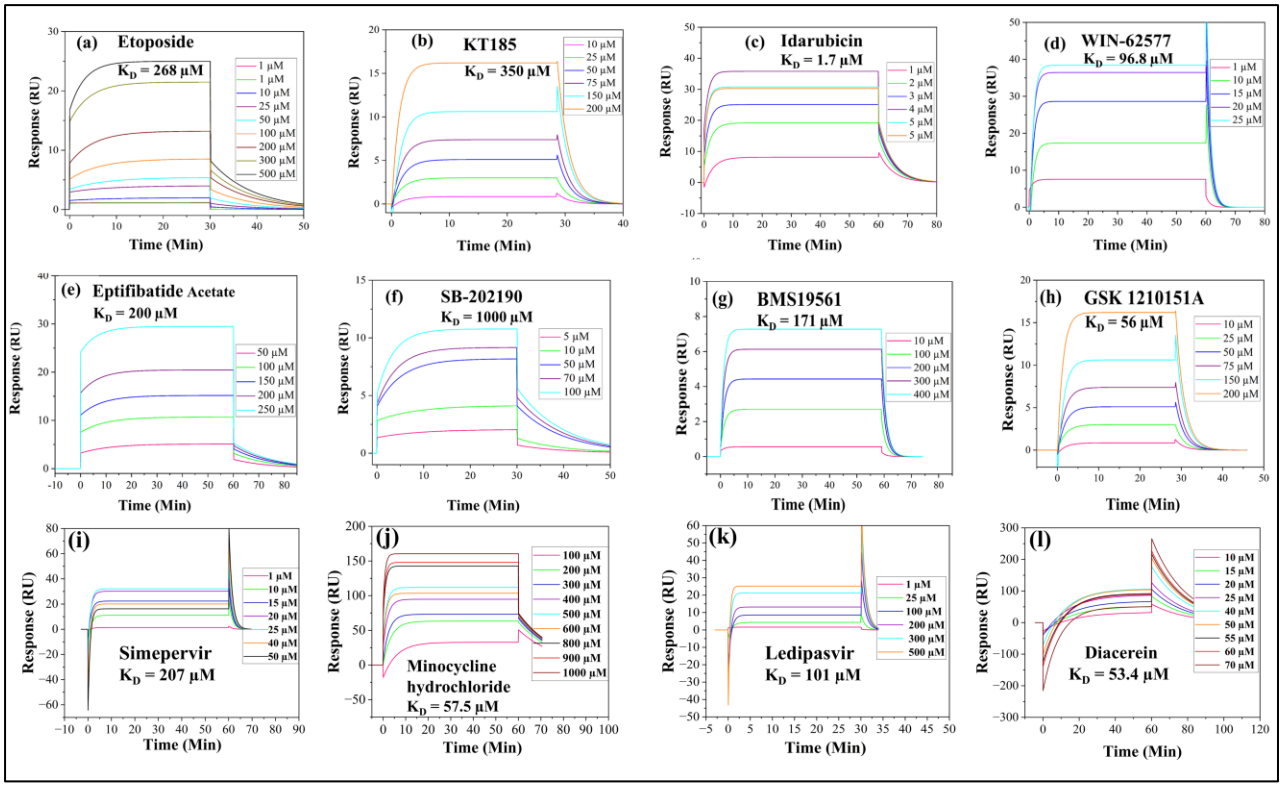

Figure 2. The SPR sensograms for the selected compounds, illustrating direct binding of in silico identified molecules to purified SARS-CoV-2 Mpro protein. The binding kinetics affinities (K_D) between the inhibitors and Mpro were analyzed using a Biacore T200, assuming steady-state and 1:1 single interaction models. Various concentrations of the compounds were injected into the system, with each concentration represented by different colors in the subgraphs.

Thermodynamics reveal that presence of inhibitors decreases the stability of Mpro dimer. In an ITC dilution experiment,[48] heat changes was observed upon concentrated solution injected into the calorimeter cell containing initially buffer, followed by injections of more dilute solutions. The heat change results from dimers in the higher-concentration solution dissociating into monomers upon entering the lower-concentration environment. The binding constant obtained from dimer-monomer equilibrium analysis of Mpro was analysed (K_D = 1.4 ±0.9 µM) [Figure 3(a) and Table 2]. The comparison of ITC binding constant helped to analyse the effect of compounds on dimer-monomer equilibrium of Mpro (Table 2). The ITC binding constant suggests that the selected compounds are able to disturb the dimer-monomer equilibria

of Mpro by a factor of 3 to 40 folds [Figure 3 (b-f) and Table 2]. Data were processed using the Origin software provided with the instrument at 25 °C. The data were analysed using commercially available Origin7.0 associated with Microcal-ITC200 analysis Software.

Table 2. The thermodynamic parameters analysis obtained from ITC dilution experiment for selected compounds for Mpro protein.

S.No.	Protein/Compounds	n	K_D (µM)	$K_A(M^{-1})$	ΔH(cal/mol)	ΔS(cal/mol/degree)
1	$Mpro^{WT}$	1	1.4 ±0.9	$(7.0)10^5 \pm (6.6)10^4$	$(6.7)10^4 \pm (8.6)10^3$	252
2	$Mpro^{WT}$ with Bexarotene	2	58.8±0.7	$(1.7)10^4 \pm (1.3)10^4$	$(2.5)10^5 \pm 479$	-552
3	$Mpro^{WT}$ with Minocycline	2	28.5±2.8	$(3.5)10^4 \pm (1.0)10^3$	$(4.7)10^5 \pm 777$	$(-5.5)10^3$
4	$Mpro^{WT}$ with Simeprevir	2	27±1.0	$(3.7\pm)10^4 \pm 994$	$(4.2)10^5 \pm 609$	$(-2.2)10^3$
5	$Mpro^{WT}$ with Ledipasvir	1	13.5±2.4	$(7.4)10^4 \pm (1.8)10^4$	$(-1.5)10^5 \pm 16$	$(-8.8)10^3$
6	$Mpro^{WT}$ with Bexarotene	1	5.2±0.4	$(1.9)10^5 \pm (7.9)10^4$	$(2.2)10^5 \pm (6.9)10^3$	95.4
7	$Mpro^{WT}$ with Diacerein	1	4.0±0.1	$(2.5)10^5 \pm (4.9)10^4$	$(3.7)10^4 \pm (1.8)10^4$	150

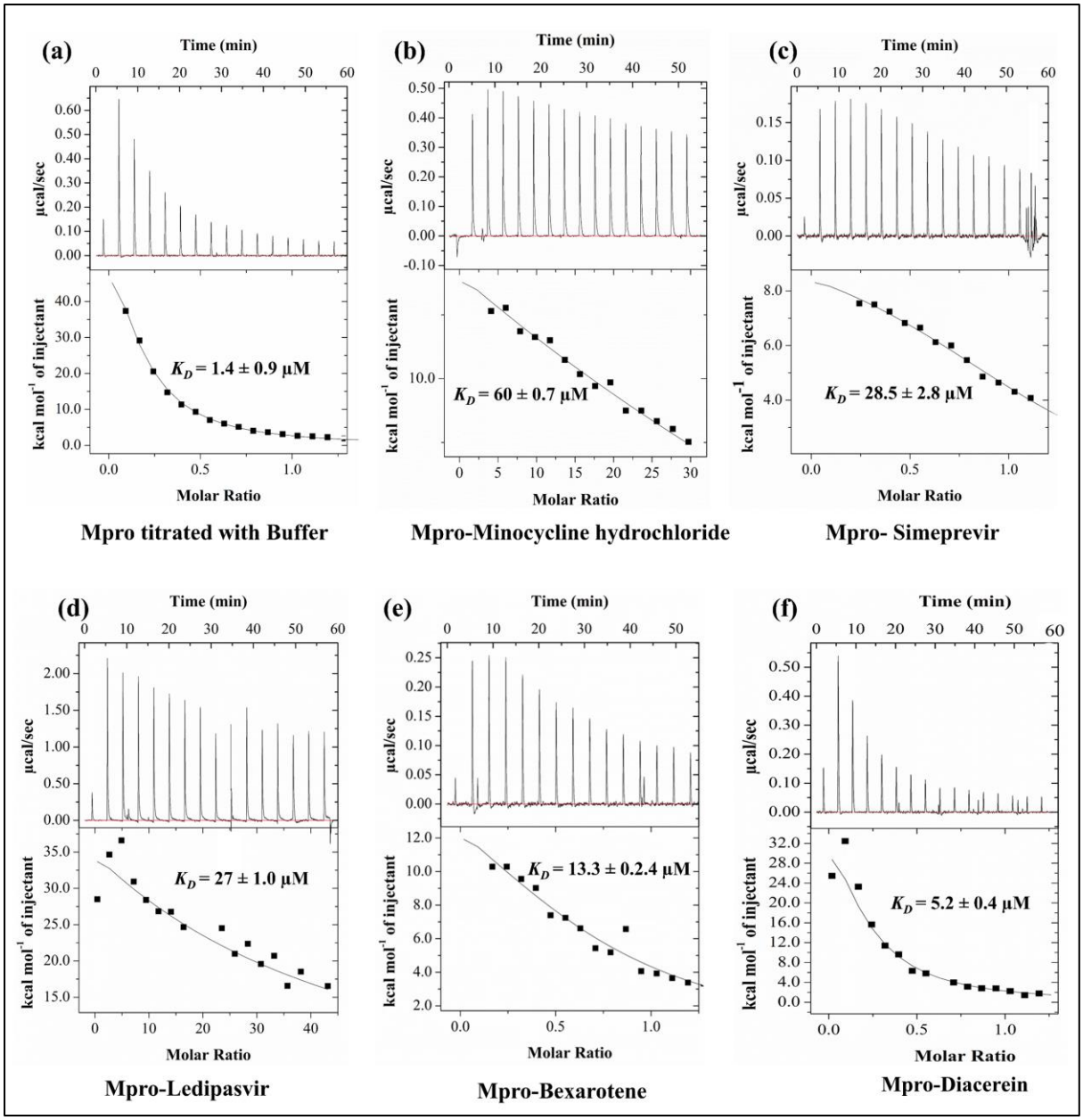

Figure 3. Binding isotherms for the monomer-dimer equilibrium of Mpro [Figure 3(a)] were determined using ITC, reflecting the changes in monomer-dimer equilibrium of Mpro in the presence of the selected compounds [Figure 3(b-f)].

FRET-based enzymatic assay for inhibition of Mpro. An *in vitro* FRET-based protease assay was developed to determine selected compounds' half-maximal inhibitory concentrations (IC_{50}) following the experimental biophysical validation of their binding energies with Mpro. For this experiment, recombinant Mpro protein was expressed in BL21 (DE3) competent cells and purified using affinity chromatography [Supporting information, Figure S2(a)]. The enzymatic activity of Mpro was assessed using the fluorogenic peptide substrate Dabcyl-AVLQ↓SGFR-Glu-Edans (Biolinkk, India). The FRET assay revealed IC_{50} values for etoposide, KT185, idarubicin, WIN-62577, eptifibatide acetate, BMS195614, GSK183870A, diacerein, simeprevir, ledipasvir, bexarotene, and minocycline hydrochloride as 0.3010 ± 0.2626 µM, 0.08591 ± 0.0420 µM, 0.2504 ± 0.1486 µM, 7.31 ± 0.927 µM, 0.1154 ± 0.09 µM, 0.2823 ± 0.012 µM, 0.496 ± 0.5026 µM, 2.85 ± 1.5 µM, 3.8 ± 0.5 µM, 5.65 ± 0.8 µM, 7.82 ± 0.65 µM, and 11.98 ± 2.15 µM, respectively (Figure 4). Compounds

KT203, SB202190, and linopiridine did not show any significant effect in inhibiting the protease activity of Mpro. A serine protease inhibitory compound was used as a negative control, and no inhibitory activity was observed. Combining the SPR-based binding kinetics assay results, monomer-dimer equilibria analysis using ITC, and the FRET-based protease assay, the top twelve selected

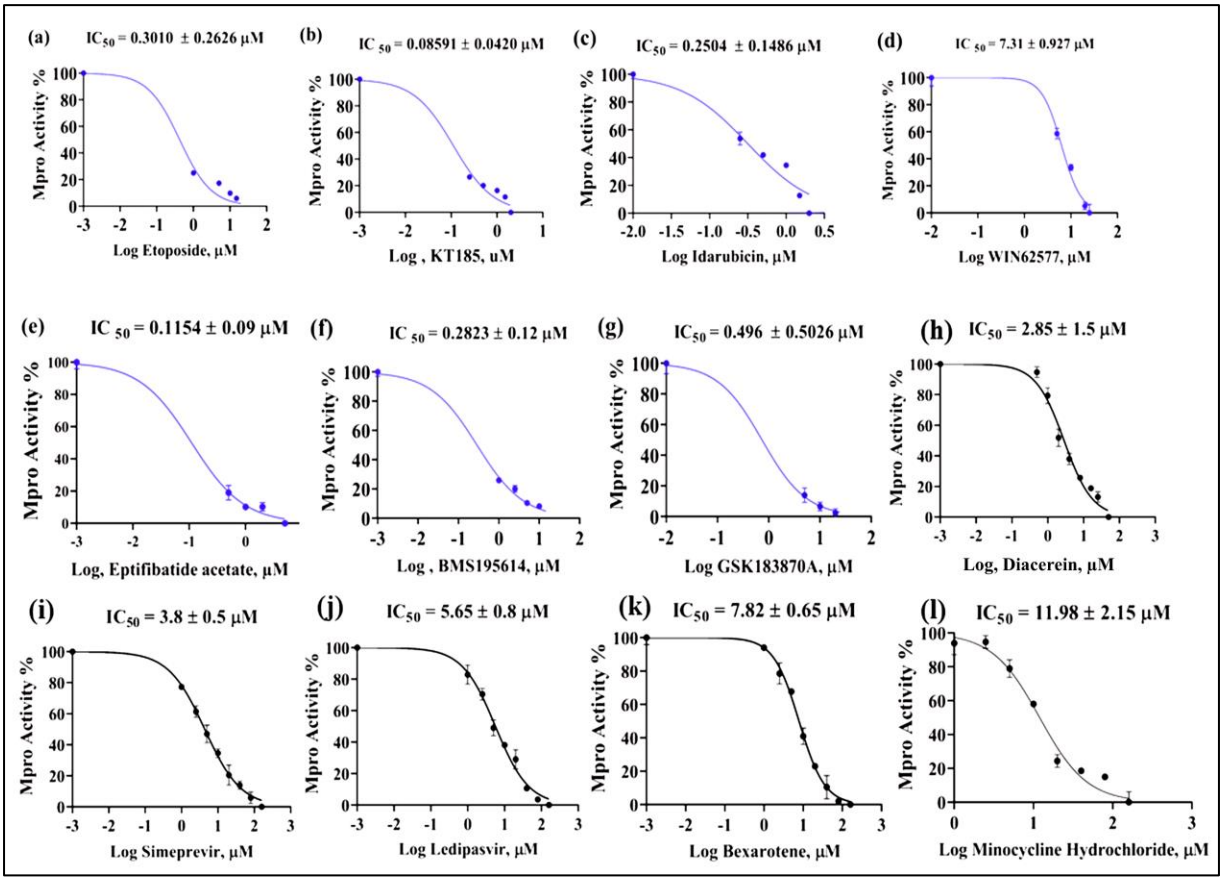

compounds were used for a cell culture-based antiviral assay.

Figure 4. The dose-response curves illustrating the inhibitory concentration (IC_{50}) of specific compounds against SARS-CoV-2 Mpro in the FRET assay were examined for enzymatic inhibition. The inhibition of SARS-CoV-2 Mpro enzyme activity by the identified compounds (a) Etoposide, (b) KT185, (c) Idarubicin, (d) WIN62577, (e) Eptifibatide Acetate, (f) BMS195614, (g) GSK183870A (h) Diacerein, (i) Simeprevir, (j) Ledipasvir, (k) Bexarotene, and (l) Minocycline hydrochloride was assessed using an in-vitro fluorescence resonance energy transfer (FRET) assay. The data presented as the mean ± standard deviation (SD) from triplicate experiments. Dose-response curves from fig (a-g) are shown with blue color whereas (h-l) are shown with black color.

Antiviral efficacy of Mpro inhibitors. After 48 hours of infection and compound treatment, the plate was freeze-thawed, and qRT-PCR quantified the viral RNA present in the cell lysate to evaluate the antiviral effect of potential compounds by considering virus control as 100% replication of the virus. Out of twelve compounds which were evaluated for anti-SARS-CoV-2 activity, six compounds, WIN-62577, KT185, bexarotene, ledipasvir, diacerein, and simepervir have significantly reduced the replication of SARS-CoV-2 in Vero cells with EC_{50} values ranges from 1.80 – 18.92 µM [Figure 5(a-f)]. Eptifibatide Acetate, BMS-195614,

SB202190, and prulifloxacin have not shown significant anti-SARS-CoV-2 activity. Etoposide and idarubicin were highly toxic at low concentrations and were unable to reduce SARS-CoV-2 replication at non-cytotoxic concentrations (Supporting information, Figure S5).

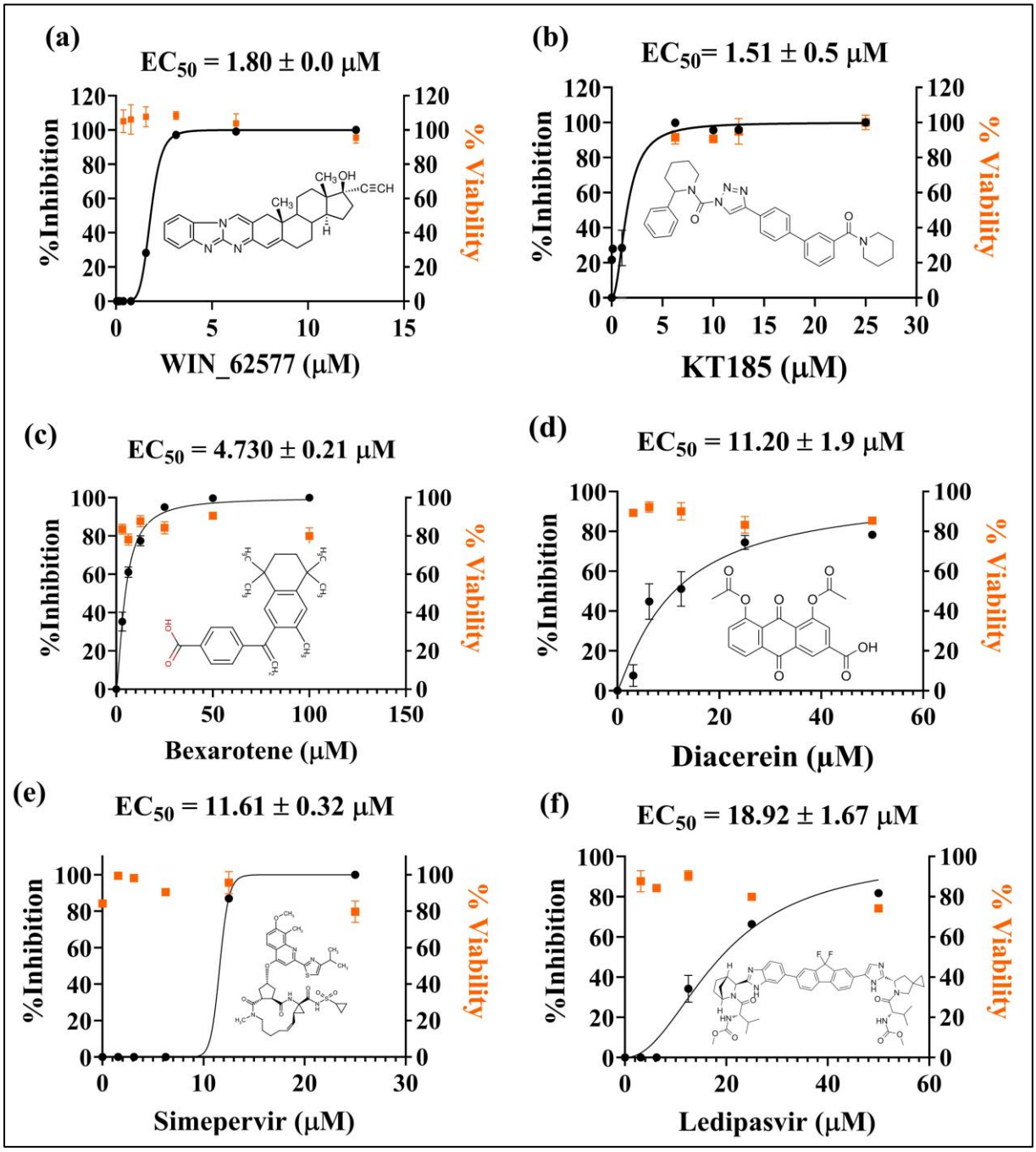

Figure 5. The antiviral efficacy of prospective drug compounds against SARS-CoV-2. Percentage inhibition and viability graphs for the compounds are presented. Duplicate wells of cells were treated with the compounds for 3 hours before being infected with SARS-CoV-2 at a multiplicity of infection (MOI) of 0.01. The percentage inhibition of virus replication in the presence of the compounds was determined using qRT-PCR, comparing the ΔΔCt values to those of the virus control (untreated cells). The values shown are means, with error bars representing the standard deviation between duplicate wells, calculated using GraphPad Prism. Graphs. Results are displayed as mean values with standard error of the mean (s.e.m.), based on three biological replicates (n = 3).

Crystal structure of Mpro-Minocycline complex. The Mpro-minocycline complex was determined at a resolution of 2.7 Å in the *P* 2_1 2_1 2_1 space group (Table 3). The Mpro-minocycline complex crystal structure consists of two molecules in an asymmetric unit [Figure 6(a)]. The monomeric unit of Mpro comprises three domains (I, II, and III) [Figure 6(b)], domain III and I interact within a two-fold asymmetric unit to form a homodimer. The crystallographic data shows that the minocycline molecule was modelled and refined with full occupancy in the allosteric site of Mpro in chain A, where it fits well into the observed electron density [Figure 6(c)]. A superimposition of the Mpro-minocycline complex with apo-Mpro shows an RMSD of 0.80 Å, based on the alignment of 245 Cα atoms. Although the low resolution of the structure limits precise analysis of the ligand position and the conformational flexibility of Mpro in response to ligand interactions, the crystal structure of the Mpro-minocycline complex provides valuable insights into the molecular interactions that contribute to its instability, especially its interaction with Mpro. Minocycline establishes hydrogen bonds with Lys236, Tyr237, and Gln238 in protomer A, whereas minocycline engages in hydrophobic interactions with Tyr239, Leu272, Gln273, Asn274, and Gly275 in promoter A of the homodimer [Figure 6(d)].

Table 3. Data collection and refinement statistics from X-ray crystallography

Crystal	**Mpro-Minocycline (PDB Id-9J19)**
Data collection	
Space group	*P* 2_1 2_1 2_1
Unit cell dimensions	
a, b, c (Å)	67.9 90.7 101.3
Resolution range	23.16 - 2.7 (2.796 - 2.7)
Unique reflections	17689 (1720)
Multiplicity	10.5 (11.0)
Completeness (%)	99.07 (99.94)
Mean I/sigma(I)	13.2 (3.1)
Wilson B-factor	32.3
R-merge	0.18 (0.69)
R-meas	0.19 (0.72)
R-pim	0.060 (0.21)
CC1/2	0.99 (0.90)
Refinement	
R-work† / R-free†	0.24 (0.28)/ 0.31 (0.29)
Number of non-hydrogen atoms	4568
macromolecules	4535
ligands	33
Protein residues	584

RMS(bonds)	0.008
RMS(angles)	1.4
Ramachandran favoured (%)	93.3
Ramachandran allowed (%)	6.0
Ramachandran outliers (%)	0.5
Clashscore	4.7
Average B-factor	38.7
macromolecules	38.5
Ligands	67.6

*Statistics for the highest-resolution shell are shown in parentheses.

[#]Rmerge =100 $\times\Sigma_{hkl}\,\Sigma_i\,|I_i(hkl) - \langle I(hkl)\rangle\,| \,/\, \Sigma_{hkl}\,\Sigma_i I_i(hkl)$, where $I(hkl)\rangle$ is the mean value of I(*hkl*).

[†] R_{work} =100 $\times\Sigma_{hkl}\,||F_o| - |F_c|\,| \,/\, \Sigma_{hkl}\,|F_o|$, where F_o and F_c are the observed and calculated structure factors, respectively.

[‡] R_{free} is calculated for the test set comprising 5 % reflections that are not used in refinement.

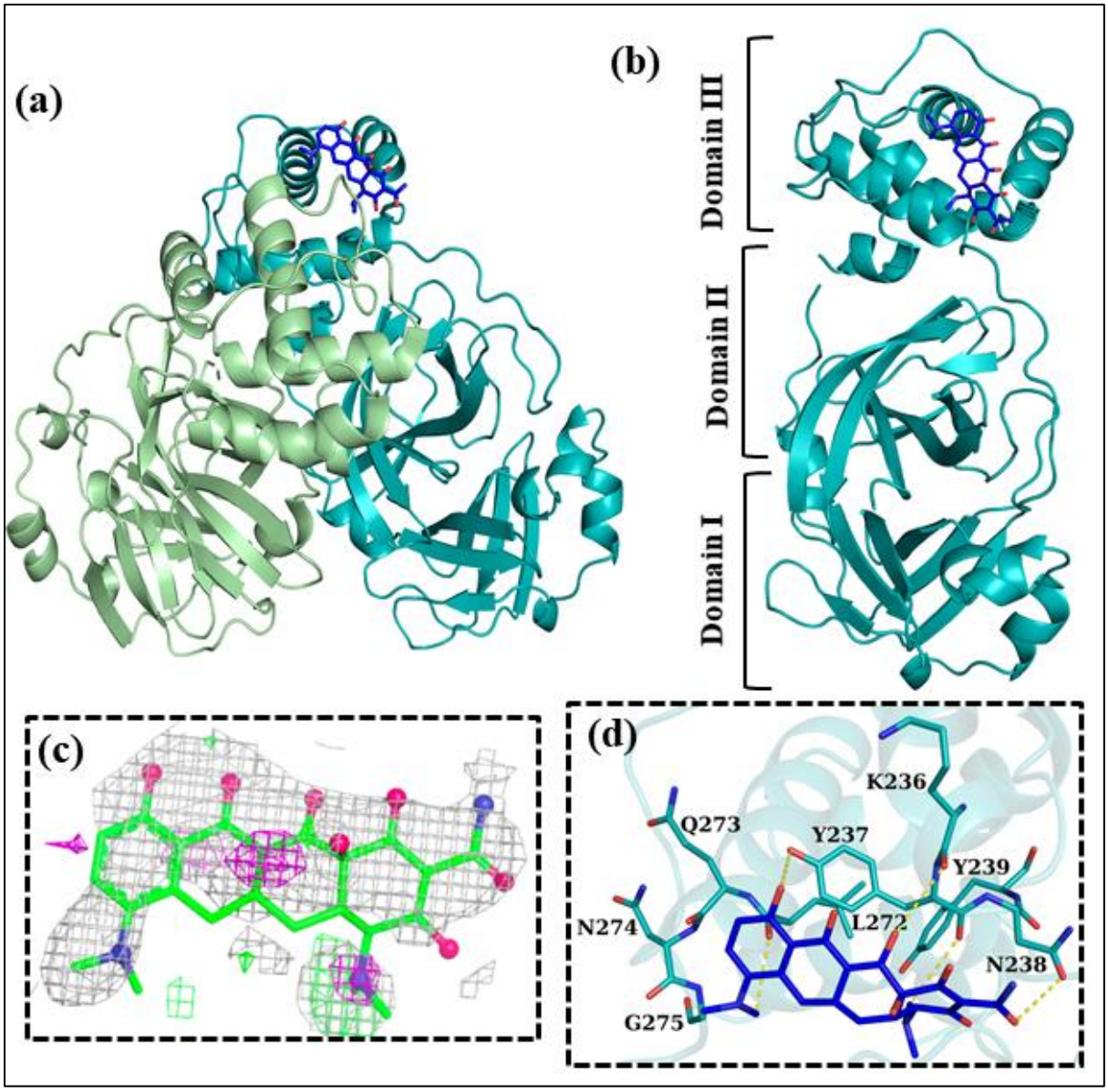

Figure 6. The crystal structure of Mpro-Minocycline complex. (a) Cartoon representation of the dimeric Mpro–inhibitor complex. (b) Cartoon representation of one protomer from Mpro–inhibitor complex. Surface representation of the Mpro homodimer, with protomer A in firebrick and protomer B in blue; Minocycline is depicted as yellow spheres. (c) Electron density map of minocycline, with Fo-Fc contoured at 3σ in green (positive) and $2F_o$-F_c, contoured at 0.7σ in grey. (d) An enlarged view of the allosteric site binding pocket, with key residues forming the pocket, is shown as sticks. Ligand is represented in blue colour sticks, residues involved in H-bond and hydrophobic interactions, are shown through teal color.

Structural insights into Mpro dimerization destabilization. The Mpro of SARS-CoV-2 forms a homodimer where Domain I & III of two monomers interact and arrange themselves in a perpendicular manner. The low pH and higher salt concentration reduce the activity of Mpro by destabilizing the salt bridge formation between Arg4 and Glu290, which is crucial for dimerization process.[49,50] Studies by Günther et al. (2021) and Douangamath et

al. (2020) identified that five and three of their compounds, respectively, bind to hydrophobic pockets within the C-terminal dimerization domain.[51,52] Chen et al. (2008) demonstrated that key residue Arg4, Ser10, Tyr237, Leu272, Asn277, and Glu290 are involved in the dimer interface.[53] The structural insight in the present study showed that minocycline is interacting on the surface at one of the druggable site as shown in Figure 7(a and b). In this study, the superimposition of the apo-Mpro structure (PDB ID: 7ALH) with the Mpro-minocycline complex results in the RMSD deviation of 0.80 Å [Figure 7(c)]. The aligned structure demonstrated that the residues Lys236-Tyr239, forming an α-helix, which is critical for the stabilization of the Mpro homodimer, exhibit a slight displacement towards the ligand in the Mpro-minocycline complex structure [Figure 7(d)]. The carboxyl group (COOH) of Lys236 forms H-bond with hydroxyl group (OH) minocycline, the OH group of Tyr237 forms a long-distance hydrogen bond with the OH group of minocycline, while the backbone of Tyr237 makes hydrogen bond with the NH group of minocycline. At the same time, the side chain of Asn238 forms a hydrogen bond with the COOH oxygen of minocycline. These residues are essential for the stabilization of the Mpro dimer and form a druggable site on the surface of Mpro. Additionally, interactions within the Mpro-minocycline complex seem to destabilize the C-terminal loop region (Asp295-Gln306) of Mpro, which is essential for homodimer formation. This destabilization likely explains the absence of electron density observed in this specific loop region [Figure 7(e)]. These changes cause substantial shifts in the side chains of active site residues, particularly Phe140, Ser144, Glu166, and Asp187, that may lead to impaired the protease activity of Mpro [Figure 7(f)]. Therefore, this study demonstrates that minocycline binding to Mpro induces significant alterations not only at the allosteric site but also in the active site region, significantly impairing protease activity of Mpro by disrupting its dimerization stability.

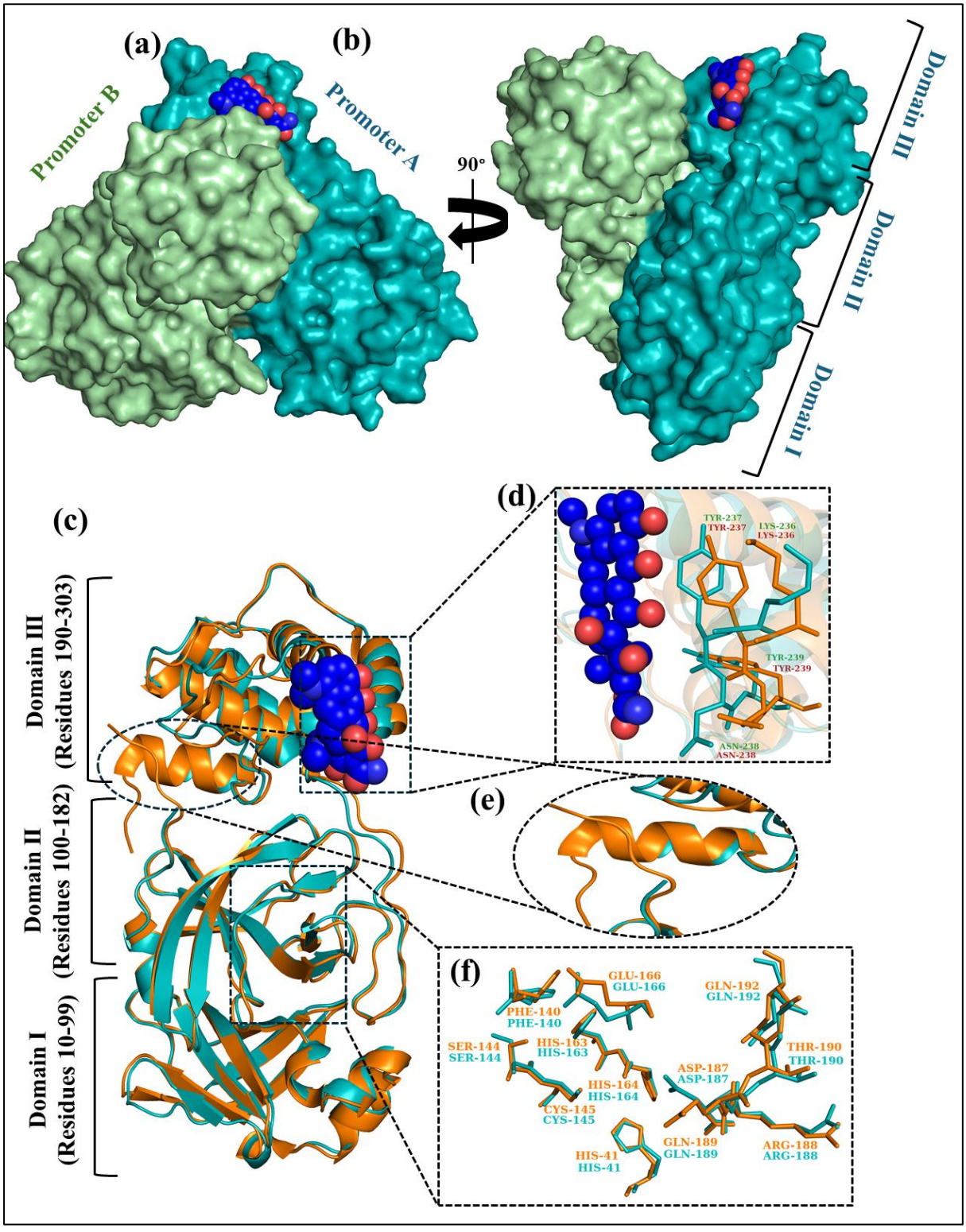

Figure 7. Schematic representation of structural superimposition of Mpro-minocycline with native-Mpro. (a) Surface representation of crystal structures of Mpro-minocycline dimer complex. (b) 90º rotation of Figure 7 (a) to show the interaction of ligand with propmoter B (c) superimposed structure of Mpro-minocycline complex with apo-Mpro structure. (d) The zoomed image represents the root-mean-square deviation (r.m.s.d. 0.80 Å) of the aligned Cα atoms. Residues 236-239 demonstrated the helical shift towards the ligand, which may cause structural destability in Mpro dimer formation.

(e) The zoomed superimposed structure showed the absence of electron density of C-terminal region in Mpro-minocycline crystal structure. This region is predominantly involved in dimer formation and stabilization of Mpro structure. (f) representation of conformational shift in active site residues due to interaction of ligand at allosteric site.

DISCUSSION

Addressing the extreme worldwide impact of the SARS-CoV-2 and evolving variants on health with their augmented transmissibility and immune evasion emphasizes the demand for effective broad-spectrum antivirals against not only the demand of effective broad-spectrum antivirals not only against SARS-CoV-2 and its variants but also against other strains of *coronaviridae* family. Mpro of SARS-CoV-2 is predominantly involved in virus replication. The conserved sequence of Mpro among the *coronaviridae* family makes it a prime target for developing effective and affordable protease inhibitors as antivirals. These target-specific inhibitor findings are leading-edge solutions and of utmost need to combat SARS-CoV-2 and its emerging highly pathogenic variants. The pharmacology-based drug repurposing process adds importance as it provides significant potential and expands new compounds against COVID-19, offering profuse opportunities for prevailing FDA-approved/ natural compounds against the highly conserved substrate binding site and dimeric interface site (allosteric site) of the Mpro. The presently reported inhibitors against Mpro protein displayed very low potency and deprived pharmacokinetic properties. Likewise, the commercially available oral antiviral Nirmatrelvir/ritonavir combination indeed has high potency against Mpro. Still, it is also responsible for causing adverse side effects, which include blurred vision, dizziness, Diarrhea, headache, nervousness, high blood pressure, pounding in the ears, chest tightness, slow or fast heartbeat, and Myalgia. Therefore, developing more potent Mpro inhibitors with minimal side effects is imperative.

Considering the previous studies and research, our prime objective was to ascertain numerous Mpro inhibitors against pan coronavirus. Implementing a target-specific strategy to gear up the drug discovery process includes the multiple sequence alignment (MSA) and structural comparison of Mpro from different strains of coronaviruses (Supporting information, Figure S6). In the current study, MSA and structural comparison showed highly conserved residues for the substrate binding pocket, including the catalytic dyad (Cys-His) and dimeric interface sites in Mpro. This observation allowed us to screen several drug libraries against target-specific pockets of Mpro. Sixteen final compounds were selected after computer-aided drug discovery approaches (Supporting information, Table S2) and subsequently employed to determine their biophysical binding affinities and kinetic studies using SPR, ITC and *in vitro* FRET-based protease assays. SPR experiments identified specific binding constants (K_D values) for the selected compounds, ranging from 1.7 to 1000 µM (Figure 2 and Table 1). The ITC binding isotherms for the top six screened compounds targeting the dimeric interface showed significant disruption of the monomer-dimer equilibrium of Mpro (Figure 3). Enzymatic inhibition assays with twelve inhibitors further confirmed their potent antiviral activity, with IC_{50} values in the low micromolar range (0.30-11.98 µM) (Figure 4). Subsequent mutational analysis of Mpro (C145A and E290A) revealed a significant reduction in both binding affinities and activity of the mutants [Supporting information, Figure S4(d)]. Previous

reports suggest that these compounds (KT185, WIN-62577, Ledipasvir, Simprevir, Bexarotene, Diacerein, and Minocycline hydrochloride) are well distinguished in their roles for treating several diseases (Supporting information, Table S11). KT185 is marketed as an oral α/β-Hydrolase domain containing 6 (ABHD6) inhibitor, decreases macrophage activation and exerts an anti-inflammatory effect on the lungs. Some *in vivo* experiments-based reports also suggest the selectivity of KT185 against liver and brain serine hydrolases. Similarly, WIN-62577 works as an allosteric enhancer of M3 muscarinic acetylcholine (Ach) receptors and is very well recognized for its anti-inflammatory properties. It also reduces bronchial smooth muscle constriction infected with Respiratory syncytial virus (RSV). Ledipasvir and Simeprevir are direct-acting antivirals (DAAs) used in combination therapy to treat chronic Hepatitis C, an infectious liver disease caused by the Hepatitis C Virus (HCV). Bexarotene, a member of the retinoid class, is used to treat cutaneous T-cell lymphoma (CTCL). Minocycline is an antibacterial agent used to treat various bacterial infections, including pneumonia, infections of the skin, eyes, lymphatic system, respiratory tract infections, intestines, genital and urinary systems, as well as certain infections transmitted by ticks, lice, mites, and infected animals as shown in (Table S11). These compounds exhibited robust biochemical inhibition of Mpro, underscoring their potential as promising candidates. Importantly, six best compounds, KT185, WIN-62577, Ledipasvir, Simprevir, Bexarotene, and Diacerein exhibited effective inhibition (EC_{50} ranges from 1.8-18.92 μM) in a comprehensive *in vitro* cell culture-based antiviral assays, exhibiting dose-dependent inhibition of viral copy numbers well below their cytotoxic threshold concentrations (Figure 5).

Previous research has demonstrated that minocycline was used alongside Favipiravir to treat COVID-19 patients in Japan during March and April of 2020.[54] Consequently, Minocycline has been recognized for its anti-inflammatory and antiviral properties, in addition to its broad-spectrum antibacterial effects.[54–56] In the present study, the crystal structure of Mpro-minocycline complex revealed binding at a druggable site near the dimeric interface of Mpro [Figure 6(a, b, and d)]. The complex displayed a conformational deviation with an RMSD value of 0.80 Å compared to its apo structure (Figure 7). Mpro contains six experimentally confirmed allosteric sites, including the dimeric interface site.[21,51] A druggability score (D-score) of ≥1.0 enabled these sites to be classified as druggable, and based on their D-scores, these sites were further ranked accordingly.[58] The crystal structure of the Mpro-minocycline complex revealed that minocycline binds to the surface of one protomer at domain 3 via long-distance hydrogen bonds which overlapped with a druggable site (highest ranking site) on Mpro located near the dimerization region but distant from the active site. The key residues (Lys236, tyr237, Asn238, and Tyr239) involved in the interaction with minocycline play a crucial role in stabilizing the dimeric structure of Mpro.[53] The alignment of the Mpro-minocycline complex with the apo structure of Mpro provided valuable insights into the conformational changes induced by minocycline binding. There is a significant shift in the helical region of domain III [Figure 7(d)], which stabilizes Mpro dimerization and facilitates the formation of an allosteric site. This site allows compounds to bind and induce conformational changes in the key residues (Phe140, Ser144, Glu166, and Asp187) of substrate-binding region [Figure 7(f)], making it more difficult for the substrate to interact with Mpro, thereby possibly impairing Mpro's activity. In summary, the present study highlights the KT185, WIN-62577, ledipasvir,

simprevir, bexarotene, diacerein, and minocycline hydrochloride as potential antiviral compounds against the highly conserved substrate-binding pocket of target Mpro of SARS-CoV-2. The identified compounds display promising avenues for COVID-19 treatment and incapacitate the problems of virus mutagenesis. Given the high conservation of Mpro across coronaviruses, these inhibitors may prove to be the new age of inhibitors against SARS-CoV-2 and its potential variants as we anticipate and prepare for the next pandemic.

ASSOCIATED CONTENT

Supporting Information.

Multiple sequence alignment (MSA) of cleavage site between different non-structural proteins (Figure S1). Schematic representation of SDS-PAGE profiling of purified proteins and FRET analysis of Mpro native and mutants (Figure S2). Two-dimensional schematic representations of the interactions between screened drug molecules against substrate-binding pocket (Figure S3). MD simulation study of Mpro and Mpro-inhibitor complexes (Figure S4). Antiviral activity of compounds (Figure S5). Multiple sequence alignment (MSA) of the binding pocket of Mpro of different SARS-CoV-2 and SARS-CoV strains (Figure S6). Binding energy, inhibition constant (ki), H-bond interactions & hydrophobic interactions obtained from docking of Pep1 to Pep11 octapeptides into the catalytic site of Mpro (PDB ID: 6LU7) protein (Table S1). Binding energy, H-bond interactions & hydrophobic interactions obtained from docking of top sixteen compounds against the catalytic site (S. No:1-10) and dimeric interface (S.No: 11-16) of Mpro (PDB ID: 6LU7) protein (Table S2). P1 residue of octapeptides interacting with S1 subsite of Mpro (Table S3). P2 residue of octapeptides interacting with S2 subsite of Mpro (Table S4). P3 residue of octapeptides interacting with S3 subsite of Mpro (Table S5). P4 residue of octapeptides interacting with S4 subsite of Mpro (Table S6). P1' residue of octapeptides interacting with S1' subsite of Mpro (Table S7). P2' residue of octapeptides interacting with S2' subsite of Mpro (Table S8). P3' residue of octapeptides interacting with S3' subsite of Mpro (Table S9). P4' residue of octapeptides interacting with S4' subsite of Mpro (Table S10). Identified potential drug molecules with their known functions (table S11).

Accession Code

SARS CoV-2 nsP5 [Main protease (Mpro)], UniProtKB P0DTD1 (R1AB_SARS2).

DECLARATION

Ethics approval and consent to participate. Not applicable

Consent for publication. All authors give their consent for submission and publication of this manuscript.

Availability of data and material. The coordinates and structure factors for the SARS-CoV-2 Mpro in complex with the inhibitor minocycline have been deposited in the PDB under accession number 9J19, with the deposit made on August 4, 2024, and released on August 8, 2024. Any other pertinent data can be obtained from the corresponding authors upon reasonable request.

Competing interests. Not applicable

Funding. Science and Technology Award for Research - Intensification of Research in High Priority Area (Grant No.- IPA/2020/000054), Government of India.

AUTHOR INFORMATION

Corresponding authors*

***Shailly Tomar**- Professor, Department of Biosciences and Bioengineering, Indian Institute of Technology Roorkee, Uttarakhand (247667), India;
ORCID ID: 0000-0002-1730-003X;
Email: shailly.tomar@bt.iitr.ac.in

***Pravindra Kumar**- Professor, Department of Biosciences and Bioengineering, Indian Institute of Technology Roorkee, Uttarakhand (247667), India;
ORCID ID: 0000-0003-2128-7736;
Email: pravindra.kumar@bt.iitr.ac.in

***Gaurav Kumar Sharma**
Senior scientist, Indian Veterinary Research Institute, Izatnagar, Bareilly, Uttar Pradesh state (243122), India;
ORCID ID: 0000-0002-9996-9422;
Email: gaurvet@gmail.com

Authors

Ankur Singh- Department of Biosciences and Bioengineering, Indian Institute of Technology Roorkee, Roorkee, Uttarakhand - 247667, India;

Kuldeep Jangid- Department of Biosciences and Bioengineering, Indian Institute of Technology Roorkee, Roorkee, Uttarakhand - 247667, India;

Sanketkumar Nehul- Department of Biosciences and Bioengineering, Indian Institute of Technology Roorkee, Roorkee, Uttarakhand - 247667, India;

Preeti Dhaka- Department of Biosciences and Bioengineering, Indian Institute of Technology Roorkee, Roorkee, Uttarakhand - 247667, India;

Ruchi Rani- Department of Biosciences and Bioengineering, Indian Institute of Technology Roorkee, Roorkee, Uttarakhand - 247667, India;

Akshay Pareek- Department of Biosciences and Bioengineering, Indian Institute of Technology Roorkee, Roorkee, Uttarakhand - 247667, India;

Authors' contributions. ST, PK & GK: Conception and design, interpretation of data, review of the manuscript, and study supervision. AS, KD, SN, PD, RR, & AP: Acquisition and interpretation of data, & writing of the manuscript.

ACKNOWLEDGEMENTS

This research was funded by Science and Engineering Research Board, Department of Science & Technology, the Government of India (Proj. ref no. IPA/2020/000054). PK and ST thank Department of Biotechnology, Govt of India for supporting Bioinformatics Centre at IIT Roorkee (reference number BT/PR40141/BTIS/137/16/2021). A.S, K.D., S.N., & P.D. acknowledges the Ministry of Human Resource Development, (MHRD). R.R thanks

University Grants Commission (UGC), Government of India for research fellowship. A.P thanks the Council of Scientific & Industrial Research (CSIR), Government of India for financial support. The authors acknowledge and thank the Macromolecular Crystallographic Facility (MCU) at Institute Instrumentation Centre (IIC), BSL3 facility at Indian Institute of Technology, Roorkee, and BSL3 facility of Indian Veterinary Research Institute, Izatnagar, Bareilly.

AS, KD, SN, PD, RR, AP, PK, GK, and ST thanks University Grants Commission, Ministry of Human Resource Development and Council of Scientific & Industrial Research, and Science and Technology Award for Research - Intensification of Research in High Priority Area (Grant No.- IPA/2020/000054), Government of India for financial support. Authors thank Macromolecular Crystallographic Facility (MCU) at the Indian Institute of Technology Roorkee (IIT Roorkee).

Conflicts of interest. The authors declare that they have no conflicts of interest.

References

(1) Aleanizy, F. S., Mohmed, N., Alqahtani, F. Y., and El Hadi Mohamed, R. A. (2017) Outbreak of Middle East respiratory syndrome coronavirus in Saudi Arabia: A retrospective study. *BMC Infectious Diseases 17*.
(2) de Groot, R. J., Baker, S. C., Baric, R. S., Brown, C. S., Drosten, C., Enjuanes, L., Fouchier, R. A. M., Galiano, M., Gorbalenya, A. E., Memish, Z. A., Perlman, S., Poon, L. L. M., Snijder, E. J., Stephens, G. M., Woo, P. C. Y., Zaki, A. M., Zambon, M., and Ziebuhr, J. (2013) Commentary: Middle East Respiratory Syndrome Coronavirus (MERS-CoV): Announcement of the Coronavirus Study Group. *Journal of Virology 87*, 7790–7792.
(3) Su, S., Wong, G., Shi, W., Liu, J., Lai, A. C. K., Zhou, J., Liu, W., Bi, Y., and Gao, G. F. (2016) Epidemiology, Genetic Recombination, and Pathogenesis of Coronaviruses. *Trends in microbiology 24*, 490–502.
(4) Wang, L. F., Shi, Z., Zhang, S., Field, H., Daszak, P., and Eaton, B. T. (2006) Review of bats and SARS. *Emerging infectious diseases 12*, 1834–1840.
(5) Zhong, N. S., Zheng, B. J., Li, Y. M., Poon, L. L. M., Xie, Z. H., Chan, K. H., Li, P. H., Tan, S. Y., Chang, Q., Xie, J. P., Liu, X. Q., Xu, J., Li, D. X., Yuen, K. Y., Peiris, J. S. M., and Guan, Y. (2003) Epidemiology and cause of severe acute respiratory syndrome (SARS) in Guangdong, People's Republic of China, in February, 2003. *Lancet 362*, 1353–1358.
(6) Lefkowitz, E. J., Dempsey, D. M., Hendrickson, R. C., Orton, R. J., Siddell, S. G., and Smith, D. B. (2018) Virus taxonomy: The database of the International Committee on Taxonomy of Viruses (ICTV). *Nucleic Acids Research 46*, D708–D717.
(7) Dhawan, M., Saied, A. R. A., Mitra, S., Alhumaydhi, F. A., Emran, T. Bin, and Wilairatana, P. (2022) Omicron variant (B.1.1.529) and its sublineages: What do we know so far amid the emergence of recombinant variants of SARS-CoV-2? *Biomedicine & Pharmacotherapy 154*, 113522.
(8) Willett, B. J., Grove, J., MacLean, O. A., Wilkie, C., De Lorenzo, G., Furnon, W., Cantoni, D., Scott, S., Logan, N., Ashraf, S., Manali, M., Szemiel, A., Cowton, V., Vink, E., Harvey, W. T., Davis, C., Asamaphan, P., Smollett, K., Tong, L., Orton, R. J., Hughes, J., Holland, P., Silva, V., Pascall, D. J., Puxty, K., da Silva Filipe, A., Yebra, G., Shaaban, S., Holden, M. T. G., Pinto, R. M., Gunson, R., Templeton, K., Murcia, P. R., Patel, A. H., Klenerman, P., Dunachie, S., Klenerman, P., Barnes, E., Brown, A., Adele, S., Kronsteiner, B., Murray, S. M., Abraham, P., Deeks, A., Ansari, M. A., de Silva, T., Turtle, L., Moore, S., Austin, J., Richter, A., Duncan, C., Payne, R., Ash, A., Koshy, C., Kele, B., Cutino-Moguel, T., Fairley, D. J., McKenna, J. P., Curran, T., Adams, H., Fraser, C., Bonsall, D., Fryer, H., Lythgoe, K., Thomson, L., Golubchik, T., Murray, A., Singleton, D., Beckwith, S. M., Mantzouratou, A., Barrow, M., Buchan, S. L., Reynolds, N., Warne, B., Maksimovic, J., Spellman, K., McCluggage, K., John, M., Beer, R., Afifi, S., Morgan, S., Mack, A., Marchbank, A., Price, A., Morriss, A., Bresner, C., Kitchen, C., Merrick, I., Southgate, J., Guest, M., Jones, O., Munn, R., Connor, T. R., Whalley, T., Workman, T., Fuller, W., Patel, A., Patel, B., Nebbia, G., Edgeworth, J., Snell, L. B., Batra, R., Charalampous, T., Beckett, A. H., Shelest, E., Robson, S. C., Underwood, A. P., Taylor, B. E. W., Yeats, C. A., Aanensen, D. M., Abudahab, K., Menegazzo, M., Joseph, A., Clark, G., Howson-Wells, H. C., Berry, L., Khakh, M., Lister, M. M., Boswell, T., Fleming, V. M., Holmes, C. W., McMurray, C. L., Shaw, J., Tang, J. W., Fallon, K., Odedra, M., Willford, N. J., Bird, P. W., Helmer, T., Williams, L. A., Sheriff, N., Campbell, S., Raviprakash, V., Blakey, V., Moore, C., Sang, F., Debebe, J., Carlile, M., Loose, M. W., Holmes, N., Wright, V., Torok, M. E., Hamilton, W. L., Carabelli, A. M., Jermy, A., Blane, B., Churcher, C. M., Ludden, C., Aggarwal, D., Westwick, E., Brooks, E., McManus, G. M., Galai, K., Smith, K., Smith, K. S., Cox, M. G., Fragakis, M., Maxwell, P., Judges, S., Peacock, S. J., Feltwell, T., Kenyon, A., Eldirdiri, S., Davis, T., Taylor, J. F., Tan, N. K., Zarebski, A. E., Gutierrez, B., Raghwani, J., du Plessis,

L., Kraemer, M. U. G., Pybus, O. G., Francois, S., Attwood, S. W., Vasylyeva, T. I., Jahun, A. S., Goodfellow, I. G., Georgana, I., Pinckert, M. L., Hosmillo, M., Izuagbe, R., Chaudhry, Y., Ryan, F., Lowe, H., Moses, S., Bedford, L., Cargill, J. S., Hughes, W., Moore, J., Stonehouse, S., Shah, D., Lee, J. C. D., Brown, J. R., Harris, K. A., Atkinson, L., Storey, N., Spyer, M. J., Flaviani, F., Alcolea-Medina, A., Sehmi, J., Ramble, J., Ohemeng-Kumi, N., Smith, P., Bertolusso, B., Thomas, C., Vernet, G., Lynch, J., Moore, N., Cortes, N., Williams, R., Kidd, S. P., Levett, L. J., Pusok, M., Grant, P. R., Kirk, S., Chatterton, W., Xu-McCrae, L., Smith, D. L., Young, G. R., Bashton, M., Kitchman, K., Gajee, K., Eastick, K., Lillie, P. J., Burns, P. J., Everson, W., Cox, A., Holmes, A. H., Bolt, F., Price, J. R., Pond, M., Randell, P. A., Madona, P., Mookerjee, S., Volz, E. M., Geidelberg, L., Ragonnet-Cronin, M., Boyd, O., Johnson, R., Pope, C. F., Witney, A. A., Monahan, I. M., Laing, K. G., Smollett, K. L., McNally, A., McMurray, C., Stockton, J., Quick, J., Loman, N. J., Poplawski, R., Nicholls, S., Rowe, W., Castigador, A., Macnaughton, E., Bouzidi, K. El, Sudhanva, M., Lampejo, T., Martinez Nunez, R. T., Breen, C., Sluga, G., Withell, K. T., Machin, N. W., George, R. P., Ahmad, S. S. Y., Pritchard, D. T., Binns, D., Wong, N., James, V., Williams, C., Illingworth, C. J., Jackson, C., de Angelis, D., Pascall, D., Mukaddas, A., Broos, A., Mair, D., Wright, D. W., Starinskij, I., Tsatsani, I., Shepherd, J. G., Nichols, J., Nomikou, K., Tong, L., Vattipally, S., Harvey, W. T., Sanderson, R., O'Brien, S., Rushton, S., Perkins, J., Blacow, R., Gunson, R. N., Gallagher, A., Wastnedge, E., Templeton, K. E., McHugh, M. P., Dewar, R., Cotton, S., Coupland, L., Stanley, R., Dervisevic, S., Spurgin, L. G., Smith, L., Graham, C., Padgett, D., Barton, E., Scott, G., Cross, A., Mirfenderesky, M., Swindells, E., Greenaway, J., Denton-Smith, R., Turnbull, R., Idle, G., Cole, K., Hollis, A., Nelson, A., McCann, C. M., Henderson, J. H., Crown, M. R., Yew, W. C., Stanley, W., Duckworth, N., Clarke, P., Walsh, S., Sloan, T. J., Bicknell, K., Impey, R., Wyllie, S., Elliott, S., Glaysher, S., Bradley, D. T., Killough, N. F., Wyatt, T., Bosworth, A., Vipond, B. B., Pearson, C., Allara, E., Robinson, E., Pymont, H. M., Osman, H., Muir, P., Hopes, R., Hutchings, S., Curran, M. D., Parmar, S., Thornton, A., Lackenby, A., Bishop, C., Bibby, D., Lee, D., Gallagher, E., Dabrera, G., Harrison, I., Hubb, J., Twohig, K. A., Chand, M., Ellaby, N., Manesis, N., Myers, R., Platt, S., Mbisa, T., Chalker, V., Yebra, G., Holden, M. T. G., Shaaban, S., Rooke, S., Birchley, A., Adams, A., Davies, A., Gaskin, A., Gatica-Wilcox, B., McKerr, C., Moore, C., Williams, C., Williams, C., Heyburn, D., De Lacy, E., Hilvers, E., Downing, F., Pugh, G., Jones, H., Asad, H., Coombes, J., Hey, J., Powell, J., Watkins, J., Evans, J. M., Fina, L., Gifford, L., Gilbert, L., Graham, L., Perry, M., Morgan, M., Bull, M., Pacchiarini, N., Craine, N., Corden, S., Kumziene-Summerhayes, S., Rey, S., Taylor, S., Cottrell, S., Jones, S., Edwards, S., Annett, T., Trotter, A. J., Mather, A. E., Aydin, A., Page, A. J., Baker, D. J., Foster-Nyarko, E., Kay, G. L., O'Grady, J., de Oliveira Martins, L., Meadows, L., Alikhan, N. F., Prosolek, S. J., Rudder, S., Le-Viet, T., Casey, A., Ratcliffe, L., Singh, A., Mariappan, A., Baxter, C., Radulescu, C., Simpson, D. A., Lavin, D., Rogan, F., Miskelly, J., Fuchs, M., Tang, M., Carvalho, S. F., Bridgett, S., Skvortsov, T., Molnar, Z., Ramadan, N. A., Knight, B. A., Jones, C. R., Auckland, C., Morcrette, H., Poyner, J., Irish-Tavares, D., Witele, E., Hart, J., Mahungu, T. W., Haque, T., Bourgeois, Y., Fearn, C., Cook, K. F., Loveson, K. F., Goudarzi, S., Evans, C., Partridge, D. G., Johnson, K., Yavus, M., Raza, M., Mower, C., Baker, P., Essex, S., Bonner, S., Murray, L. J., Watson, L. K., Liggett, S., Lawton, A. I., Lyons, R. A., Payne, B. A. I., Eltringham, G., Collins, J., Waugh, S., Burton-Fanning, S., Taha, Y., Jeanes, C., Gomes, A. N., Murray, D. R., Kimuli, M., Dobie, D., Ashfield, P., Best, A., Percival, B., Moles-Garcia, E., Ashford, F., Mirza, J., Crawford, L., Mayhew, M., Cumley, N., Megram, O., Frampton, D., Heaney, J., Byott, M., Houlihan, C., Williams, C. A., Nastouli, E., Lowe, H. L., Hartley, J. A., Breuer, J., Maftei, L., Ensell, L., Cotic, M., Mondani, M., Driscoll, M., Bayzid, N., Williams, R. J., Roy, S., Mahanama, A. I. K., Samaraweera, B., Wilson-Davies, E., Pelosi, E., Umpleby, H., Wheeler, H., Prieto, J. A., Saeed, K., Harvey, M., Jeremiah, S.,

Silviera, S., Aplin, S., Sass, T., Macklin, B., Crudgington, D., Sheridan, L. A., Cogger, B. J., Malone, C. S., Munemo, F., Huckson, H., Lewis, J., Easton, L. J., Mutingwende, M., Erkiert, M. J., Hassan-Ibrahim, M. O., Chaloner, N. J., Podplomyk, O., Randell, P., Nicodemi, R., Lowdon, S., Somassa, T., Richter, A., Beggs, A., Hesketh, A. R., Smith, C. P., Bucca, G., Ruis, C., Cormie, C., Higginson, E. E., Young, J., Dias, J., Kermack, L. M., Maes, M., Gupta, R. K., Forrest, S., Girgis, S. T., Davidson, R. K., O'Toole, Á., Rambaut, A., Jackson, B., Balcazar, C. E., Maloney, D., Scher, E., McCrone, J. T., Williamson, K. A., Gallagher, M. D., Medd, N., Colquhoun, R., Stanton, T. D., Williams, T., Hill, V., Jeffries, A. R., Temperton, B., Sambles, C. M., Studholme, D. J., Warwick-Dugdale, J., Jackson, L. M., Michelsen, M. L., Manley, R., Michell, S. L., Darby, A. C., Lucaci, A. O., Nelson, C., Wierzbicki, C., Vamos, E. E., Webster, H. J., Jackson, K. A., Rainbow, L., Hughes, M., Whitehead, M., Gemmell, M., Iturriza-Gomara, M., Eccles, R., Gregory, R., Haldenby, S. T., Paterson, S., Angyal, A., Keeley, A. J., Foulkes, B. H., Lindsey, B. B., Wang, D., Hornsby, H. R., Green, L. R., Pohare, M., Gallis, M., Parker, M. D., Whiteley, M., Smith, N., Wolverson, P., Zhang, P., Hansford, S. E., Hsu, S. N., Louka, S. F., de Silva, T. I., Freeman, T. M., Mori, M., Park, E. J., Hill, J. D., Dey, J., Ball, J., Chappell, J. G., McClure, P. C., Byaruhanga, T., Fanaie, A., Yaze, G., Hilson, R. A., Trebes, A., Green, A., Buck, D., MacIntyre-Cockett, G., Todd, J. A., Bassett, A. R., Whitwham, A., Langford, C. F., Rajan, D., Kwiatkowski, D., Harrison, E. M., Bronner, I. F., Tovar-Corona, J. M., Liddle, J., Durham, J., Bellis, K. L., Lewis, K., Aigrain, L., Redshaw, N. M., Davies, R. M., Moll, R. J., McCarthy, S. A., Lensing, S. V., Leonard, S., Farr, B. W., Scott, C., Beaver, C., Ariani, C. V., Weldon, D., Jackson, D. K., Betteridge, E., Tonkin-Hill, G., Johnston, I., Martincorena, I., Bonfield, J., Barrett, J. C., Sillitoe, J., Keatley, J. P., Oliver, K., James, K., Shirley, L., Prestwood, L., Foulser, L., Gourtovaia, M., Dorman, M. J., Quail, M. A., Spencer Chapman, M. H., Park, N. R., Livett, R., Amato, R., Kay, S., Goodwin, S., Thurston, S. A. J., Rajatileka, S., Gonçalves, S., Lo, S., Sanderson, T., Maclean, A., Goldstein, E. J., Ferguson, L., Tomb, R., Catalan, J., Jones, N., Haughney, J., Robertson, D. L., Palmarini, M., Ray, S., and Thomson, E. C. (2022) SARS-CoV-2 Omicron is an immune escape variant with an altered cell entry pathway. *Nature Microbiology 2022 7:8 7*, 1161–1179.

(9) Masters, P. S. (2006) The Molecular Biology of Coronaviruses. *Advances in Virus Research 66*, 193–292.

(10) Woo, P. C. Y., Huang, Y., Lau, S. K. P., and Yuen, K. Y. (2010) Coronavirus Genomics and Bioinformatics Analysis. *Viruses 2*, 1804.

(11) Cui, J., Li, F., and Shi, Z.-L. (2018) Origin and evolution of pathogenic coronaviruses. *Nature Reviews Microbiology 2018 17:3 17*, 181–192.

(12) Song, Z., Xu, Y., Bao, L., Zhang, L., Yu, P., Qu, Y., Zhu, H., Zhao, W., Han, Y., and Qin, C. (2019) From SARS to MERS, Thrusting Coronaviruses into the Spotlight. *Viruses 11*.

(13) Mukherjee, R., and Dikic, I. (2023) Proteases of SARS Coronaviruses. *Encyclopedia of Cell Biology 1*, 930.

(14) Goyal, B., and Goyal, D. (2020) Targeting the Dimerization of the Main Protease of Coronaviruses: A Potential Broad-Spectrum Therapeutic Strategy. *ACS Combinatorial Science 22*, 297–305.

(15) Razali, R., Asis, H., and Budiman, C. (2021) Structure-Function Characteristics of SARS-CoV-2 Proteases and Their Potential Inhibitors from Microbial Sources. *Microorganisms 9*.

(16) Chen, S. A., Arutyunova, E., Lu, J., Khan, M. B., Rut, W., Zmudzinski, M., Shahbaz, S., Iyyathurai, J., Moussa, E. W., Turner, Z., Bai, B., Lamer, T., Nieman, J. A., Vederas, J. C., Julien, O., Drag, M., Elahi, S., Young, H. S., and Lemieux, M. J. (2023) SARS-CoV-2 Mpro Protease Variants of Concern Display Altered Viral Substrate and Cell Host Target Galectin-

8 Processing but Retain Sensitivity toward Antivirals. *ACS Central Science 9*, 696–708.
(17) Ferreira, J. C., Fadl, S., and Rabeh, W. M. (2022) Key dimer interface residues impact the catalytic activity of 3CLpro, the main protease of SARS-CoV-2. *The Journal of Biological Chemistry 298*.
(18) Chen, H., Wei, P., Huang, C., Tan, L., Liu, Y., and Lai, L. (2006) Only one protomer is active in the dimer of SARS 3C-like proteinase. *The Journal of biological chemistry 281*, 13894–13898.
(19) Chang, G. G. (2010) Quaternary Structure of the SARS Coronavirus Main Protease. *Molecular Biology of the SARS-Coronavirus* 115.
(20) Mensah, J. O., Ampomah, G. B., Gasu, E. N., Adomako, A. K., Menkah, E. S., and Borquaye, L. S. (2022) Allosteric Modulation of the Main Protease (MPro) of SARS-CoV-2 by Casticin—Insights from Molecular Dynamics Simulations. *Chemistry Africa 5*, 1305–1320.
(21) Alzyoud, L., Ghattas, M. A., and Atatreh, N. (2022) Allosteric Binding Sites of the SARS-CoV-2 Main Protease: Potential Targets for Broad-Spectrum Anti-Coronavirus Agents. *Drug Design, Development and Therapy 16*, 2463.
(22) Günther, S., Reinke, P. Y. A., Fernández-Garciá, Y., Lieske, J., Lane, T. J., Ginn, H. M., Koua, F. H. M., Ehrt, C., Ewert, W., Oberthuer, D., Yefanov, O., Meier, S., Lorenzen, K., Krichel, B., Kopicki, J. D., Gelisio, L., Brehm, W., Dunkel, I., Seychell, B., Gieseler, H., Norton-Baker, B., Escudero-Pérez, B., Domaracky, M., Saouane, S., Tolstikova, A., White, T. A., Hänle, A., Groessler, M., Fleckenstein, H., Trost, F., Galchenkova, M., Gevorkov, Y., Li, C., Awel, S., Peck, A., Barthelmess, M., Schlünzen, F., Xavier, P. L., Werner, N., Andaleeb, H., Ullah, N., Falke, S., Srinivasan, V., Francą, B. A., Schwinzer, M., Brognaro, H., Rogers, C., Melo, D., Zaitseva-Doyle, J. J., Knoska, J., Penã-Murillo, G. E., Mashhour, A. R., Hennicke, V., Fischer, P., Hakanpaä¨, J., Meyer, J., Gribbon, P., Ellinger, B., Kuzikov, M., Wolf, M., Beccari, A. R., Bourenkov, G., Stetten, D. Von, Pompidor, G., Bento, I., Panneerselvam, S., Karpics, I., Schneider, T. R., Garcia-Alai, M. M., Niebling, S., Günther, C., Schmidt, C., Schubert, R., Han, H., Boger, J., Monteiro, D. C. F., Zhang, L., Sun, X., Pletzer-Zelgert, J., Wollenhaupt, J., Feiler, C. G., Weiss, M. S., Schulz, E. C., Mehrabi, P., Karnĭcar, K., Usenik, A., Loboda, J., Tidow, H., Chari, A., Hilgenfeld, R., Uetrech, C., Cox, R., Zaliani, A., Beck, T., Rarey, M., Günther, S., Turk, D., Hinrichs, W., Chapman, H. N., Pearson, A. R., Betzel, C., and Meents, A. (2021) X-ray screening identifies active site and allosteric inhibitors of SARS-CoV-2 main protease. *Science 372*, 642–646.
(23) Malone, B., Urakova, N., Snijder, E. J., and Campbell, E. A. (2021) Structures and functions of coronavirus replication–transcription complexes and their relevance for SARS-CoV-2 drug design. *Nature Reviews Molecular Cell Biology 2021 23:1 23*, 21–39.
(24) Jackson, C. B., Farzan, M., Chen, B., and Choe, H. (2021) Mechanisms of SARS-CoV-2 entry into cells. *Nature Reviews Molecular Cell Biology 2021 23:1 23*, 3–20.
(25) Jin, Z., Du, X., Xu, Y., Deng, Y., Liu, M., Zhao, Y., Zhang, B., Li, X., Zhang, L., Peng, C., Duan, Y., Yu, J., Wang, L., Yang, K., Liu, F., Jiang, R., Yang, X., You, T., Liu, X., Yang, X., Bai, F., Liu, H., Liu, X., Guddat, L. W., Xu, W., Xiao, G., Qin, C., Shi, Z., Jiang, H., Rao, Z., and Yang, H. (2020) Structure of Mpro from SARS-CoV-2 and discovery of its inhibitors. *Nature 2020 582:7811 582*, 289–293.
(26) Dallakyan, S., and Olson, A. J. (2015) Small-molecule library screening by docking with PyRx. *Methods in Molecular Biology 1263*, 243–250.
(27) Eberhardt, J., Santos-Martins, D., Tillack, A. F., and Forli, S. (2021) AutoDock Vina 1.2.0: New Docking Methods, Expanded Force Field, and Python Bindings. *Journal of Chemical Information and Modeling 61*, 3891–3898.
(28) Trott, O., and Olson, A. J. (2010) AutoDock Vina: Improving the speed and accuracy of docking with a new scoring function, efficient optimization, and multithreading. *Journal of*

Computational Chemistry 31, 455–461.
(29) Crooks, G. E., Hon, G., Chandonia, J. M., and Brenner, S. E. (2004) WebLogo: a sequence logo generator. *Genome research 14*, 1188–1190.
(30) Chou, K.-C. (2019) Distorted Key Theory and its Implication for Drug Development. *Current Proteomics 17*, 311–323.
(31) Schechter, I., and Berger, A. (1967) On the size of the active site in proteases. I. Papain. *Biochemical and biophysical research communications 27*, 157–162.
(32) Delano, W. L. (2002) Pymol: An open-source molecular graphics tool. *CCP4 Newsletter on Protein Crystallography* 40(1), 82–92.
(33) Morris, G. M., Ruth, H., Lindstrom, W., Sanner, M. F., Belew, R. K., Goodsell, D. S., and Olson, A. J. (2009) AutoDock4 and AutoDockTools4: Automated docking with selective receptor flexibility. *Journal of Computational Chemistry 30*, 2785–2791.
(34) Van Der Spoel, D., Lindahl, E., Hess, B., Groenhof, G., Mark, A. E., and Berendsen, H. J. C. (2005) GROMACS: Fast, flexible, and free. *Journal of Computational Chemistry*.
(35) Abraham, M. J., Murtola, T., Schulz, R., Páll, S., Smith, J. C., Hess, B., and Lindah, E. (2015) Gromacs: High performance molecular simulations through multi-level parallelism from laptops to supercomputers. *SoftwareX 1–2*, 19–25.
(36) Huang, J., Rauscher, S., Nawrocki, G., Ran, T., Feig, M., De Groot, B. L., Grubmüller, H., and MacKerell, A. D. (2016) CHARMM36m: An improved force field for folded and intrinsically disordered proteins. *Nature Methods 14*, 71–73.
(37) Hanwell, M. D., Curtis, D. E., Lonie, D. C., Vandermeerschd, T., Zurek, E., and Hutchison, G. R. (2012) Avogadro: An advanced semantic chemical editor, visualization, and analysis platform. *Journal of Cheminformatics 4*, 1–17.
(38) Dhaka, P., Singh, A., Choudhary, S., Peddinti, R. K., Kumar, P., Sharma, G. K., and Tomar, S. (2023) Mechanistic and thermodynamic characterization of antiviral inhibitors targeting nucleocapsid N-terminal domain of SARS-CoV-2. *Archives of Biochemistry and Biophysics 750*, 109820.
(39) Vonrhein, C., Flensburg, C., Keller, P., Sharff, A., Smart, O., Paciorek, W., Womack, T., and Bricogne, G. (2011) Data processing and analysis with the autoPROC toolbox. *Acta crystallographica. Section D, Biological crystallography 67*, 293–302.
(40) Vagin, A., and Teplyakov, A. (2010) Molecular replacement with MOLREP. *Acta crystallographica. Section D, Biological crystallography 66*, 22–25.
(41) Winn, M. D., Ballard, C. C., Cowtan, K. D., Dodson, E. J., Emsley, P., Evans, P. R., Keegan, R. M., Krissinel, E. B., Leslie, A. G. W., McCoy, A., McNicholas, S. J., Murshudov, G. N., Pannu, N. S., Potterton, E. A., Powell, H. R., Read, R. J., Vagin, A., and Wilson, K. S. (2011) Overview of the CCP4 suite and current developments. *Acta crystallographica. Section D, Biological crystallography 67*, 235–242.
(42) Costanzi, E., Kuzikov, M., Esposito, F., Albani, S., Demitri, N., Giabbai, B., Camasta, M., Tramontano, E., Rossetti, G., Zaliani, A., and Storici, P. (2021) Structural and Biochemical Analysis of the Dual Inhibition of MG-132 against SARS-CoV-2 Main Protease (Mpro/3CLpro) and Human Cathepsin-L. *International journal of molecular sciences 22*.
(43) Murshudov, G. N., Skubák, P., Lebedev, A. A., Pannu, N. S., Steiner, R. A., Nicholls, R. A., Winn, M. D., Long, F., and Vagin, A. A. (2011) REFMAC5 for the refinement of macromolecular crystal structures. *Acta crystallographica. Section D, Biological crystallography 67*, 355–367.
(44) Emsley, P., and Cowtan, K. (2004) Coot: model-building tools for molecular graphics. *Acta crystallographica. Section D, Biological crystallography 60*, 2126–2132.
(45) Chen, V. B., Arendall, W. B., Headd, J. J., Keedy, D. A., Immormino, R. M., Kapral, G. J., Murray, L. W., Richardson, J. S., and Richardson, D. C. (2010) MolProbity: all-atom structure validation for macromolecular crystallography. *Acta crystallographica. Section D,*

Biological crystallography 66, 12–21.
(46) Adams, P. D., Afonine, P. V., Bunkóczi, G., Chen, V. B., Davis, I. W., Echols, N., Headd, J. J., Hung, L. W., Kapral, G. J., Grosse-Kunstleve, R. W., McCoy, A. J., Moriarty, N. W., Oeffner, R., Read, R. J., Richardson, D. C., Richardson, J. S., Terwilliger, T. C., and Zwart, P. H. (2010) PHENIX: a comprehensive Python-based system for macromolecular structure solution. *Acta crystallographica. Section D, Biological crystallography 66*, 213–221.
(47) Laskowski, R. A., and Swindells, M. B. (2011) LigPlot+: multiple ligand-protein interaction diagrams for drug discovery. *Journal of chemical information and modeling 51*, 2778–2786.
(48) Nashed, N. T., Aniana, A., Ghirlando, R., Chiliveri, S. C., and Louis, J. M. (2022) Modulation of the monomer-dimer equilibrium and catalytic activity of SARS-CoV-2 main protease by a transition-state analog inhibitor. *Communications Biology 2022 5:1 5*, 1–9.
(49) Silvestrini, L., Belhaj, N., Comez, L., Gerelli, Y., Lauria, A., Libera, V., Mariani, P., Marzullo, P., Ortore, M. G., Palumbo Piccionello, A., Petrillo, C., Savini, L., Paciaroni, A., and Spinozzi, F. (2021) The dimer-monomer equilibrium of SARS-CoV-2 main protease is affected by small molecule inhibitors. *Scientific Reports 11*, 9283.
(50) Goyal, B., and Goyal, D. (2020) Targeting the Dimerization of the Main Protease of Coronaviruses: A Potential Broad-Spectrum Therapeutic Strategy. *ACS Combinatorial Science 22*, 297–305.
(51) Günther, S., Reinke, P. Y. A., Fernández-Garciá, Y., Lieske, J., Lane, T. J., Ginn, H. M., Koua, F. H. M., Ehrt, C., Ewert, W., Oberthuer, D., Yefanov, O., Meier, S., Lorenzen, K., Krichel, B., Kopicki, J. D., Gelisio, L., Brehm, W., Dunkel, I., Seychell, B., Gieseler, H., Norton-Baker, B., Escudero-Pérez, B., Domaracky, M., Saouane, S., Tolstikova, A., White, T. A., Hänle, A., Groessler, M., Fleckenstein, H., Trost, F., Galchenkova, M., Gevorkov, Y., Li, C., Awel, S., Peck, A., Barthelmess, M., Schlünzen, F., Xavier, P. L., Werner, N., Andaleeb, H., Ullah, N., Falke, S., Srinivasan, V., Francą, B. A., Schwinzer, M., Brognaro, H., Rogers, C., Melo, D., Zaitseva-Doyle, J. J., Knoska, J., Penã-Murillo, G. E., Mashhour, A. R., Hennicke, V., Fischer, P., Hakanpaä¨, J., Meyer, J., Gribbon, P., Ellinger, B., Kuzikov, M., Wolf, M., Beccari, A. R., Bourenkov, G., Stetten, D. Von, Pompidor, G., Bento, I., Panneerselvam, S., Karpics, I., Schneider, T. R., Garcia-Alai, M. M., Niebling, S., Günther, C., Schmidt, C., Schubert, R., Han, H., Boger, J., Monteiro, D. C. F., Zhang, L., Sun, X., Pletzer-Zelgert, J., Wollenhaupt, J., Feiler, C. G., Weiss, M. S., Schulz, E. C., Mehrabi, P., Karnĭcar, K., Usenik, A., Loboda, J., Tidow, H., Chari, A., Hilgenfeld, R., Uetrech, C., Cox, R., Zaliani, A., Beck, T., Rarey, M., Günther, S., Turk, D., Hinrichs, W., Chapman, H. N., Pearson, A. R., Betzel, C., and Meents, A. (2021) X-ray screening identifies active site and allosteric inhibitors of SARS-CoV-2 main protease. *Science (New York, N.Y.) 372*, 642–646.
(52) Douangamath, A., Fearon, D., Gehrtz, P., Krojer, T., Lukacik, P., Owen, C. D., Resnick, E., Strain-Damerell, C., Aimon, A., Ábrányi-Balogh, P., Brandão-Neto, J., Carbery, A., Davison, G., Dias, A., Downes, T. D., Dunnett, L., Fairhead, M., Firth, J. D., Jones, S. P., Keeley, A., Keserü, G. M., Klein, H. F., Martin, M. P., Noble, M. E. M., O'Brien, P., Powell, A., Reddi, R. N., Skyner, R., Snee, M., Waring, M. J., Wild, C., London, N., von Delft, F., and Walsh, M. A. (2020) Crystallographic and electrophilic fragment screening of the SARS-CoV-2 main protease. *Nature Communications 2020 11:1 11*, 1–11.
(53) Chen, S., Zhang, J., Hu, T., Chen, K., Jiang, H., and Shen, X. (2008) Residues on the dimer interface of SARS coronavirus 3C-like protease: dimer stability characterization and enzyme catalytic activity analysis. *Journal of biochemistry 143*, 525–536.
(54) Itoh, K., Sakamaki, I., Hirota, T., and Iwasaki, H. (2022) Evaluation of minocycline combined with favipiravir therapy in coronavirus disease 2019 patients: A case-series study. *Journal of Infection and Chemotherapy 28*, 124.

(55) Wang, Z., Nong, J., Shultz, R. B., Zhang, Z., Tom, V. J., Ponnappan, R. K., and Zhong, Y. (2017) Local delivery of minocycline from metal ion-assisted self-assembled complexes promotes neuroprotection and functional recovery after spinal cord injury. *Biomaterials 112*, 62–71.
(56) Garrido-Mesa, N., Zarzuelo, A., and Gálvez, J. (2013) Minocycline: far beyond an antibiotic. *British Journal of Pharmacology 169*, 337.
(57) Günther, S., Reinke, P. Y. A., Fernández-Garciá, Y., Lieske, J., Lane, T. J., Ginn, H. M., Koua, F. H. M., Ehrt, C., Ewert, W., Oberthuer, D., Yefanov, O., Meier, S., Lorenzen, K., Krichel, B., Kopicki, J. D., Gelisio, L., Brehm, W., Dunkel, I., Seychell, B., Gieseler, H., Norton-Baker, B., Escudero-Pérez, B., Domaracky, M., Saouane, S., Tolstikova, A., White, T. A., Hänle, A., Groessler, M., Fleckenstein, H., Trost, F., Galchenkova, M., Gevorkov, Y., Li, C., Awel, S., Peck, A., Barthelmess, M., Schlünzen, F., Xavier, P. L., Werner, N., Andaleeb, H., Ullah, N., Falke, S., Srinivasan, V., Francą, B. A., Schwinzer, M., Brognaro, H., Rogers, C., Melo, D., Zaitseva-Doyle, J. J., Knoska, J., Penã-Murillo, G. E., Mashhour, A. R., Hennicke, V., Fischer, P., Hakanpaä¨, J., Meyer, J., Gribbon, P., Ellinger, B., Kuzikov, M., Wolf, M., Beccari, A. R., Bourenkov, G., Stetten, D. Von, Pompidor, G., Bento, I., Panneerselvam, S., Karpics, I., Schneider, T. R., Garcia-Alai, M. M., Niebling, S., Günther, C., Schmidt, C., Schubert, R., Han, H., Boger, J., Monteiro, D. C. F., Zhang, L., Sun, X., Pletzer-Zelgert, J., Wollenhaupt, J., Feiler, C. G., Weiss, M. S., Schulz, E. C., Mehrabi, P., Karnĭcar, K., Usenik, A., Loboda, J., Tidow, H., Chari, A., Hilgenfeld, R., Uetrech, C., Cox, R., Zaliani, A., Beck, T., Rarey, M., Günther, S., Turk, D., Hinrichs, W., Chapman, H. N., Pearson, A. R., Betzel, C., and Meents, A. (2021) X-ray screening identifies active site and allosteric inhibitors of SARS-CoV-2 main protease. *Science 372*, 642–646.
(58) Schrödinger - Physics-based Software Platform for Molecular Discovery & Design.